

X-ray and Sunyaev-Zel’dovich scaling relations in galaxy clusters

Andrea Morandi^{1*}, Stefano Ettori², Lauro Moscardini^{1,3}

¹ *Dipartimento di Astronomia, Università di Bologna, via Ranzani 1, I-40127 Bologna, Italy*

² *INAF-Osservatorio Astronomico di Bologna, via Ranzani 1, I-40127 Bologna, Italy*

³ *INFN, Sezione di Bologna, viale Berti Pichat 6/2, I-40127 Bologna, Italy*

ABSTRACT

We present an analysis of the scaling relations between X-ray properties and Sunyaev-Zel’dovich (SZ) parameters for a sample of 24 X-ray luminous galaxy clusters observed with Chandra and with measured SZ effect. These objects are in the redshift range 0.14–0.82 and have X-ray bolometric luminosity $L \gtrsim 10^{45}$ erg s^{−1}, with at least 4000 net counts collected for each source. We perform a spatially resolved spectral analysis and recover the density, temperature T and pressure profiles of the intra-cluster medium (ICM), just relying on the spherical symmetry of the cluster and the hydrostatic equilibrium hypothesis. The combined analysis of the SZ and X-ray scaling relations is a powerful tool to investigate the physical properties of the clusters and their evolution in redshift, by tracing out their thermodynamical history. We observe that the correlations among X-ray quantities only are in agreement with previous results obtained for samples of high- z X-ray luminous galaxy clusters. On the relations involving SZ quantities, we obtain that they correlate with the gas temperature with a logarithmic slope significantly larger than the predicted value from the self-similar model. The measured scatter indicates, however, that the central Compton parameter y_0 is a proxy of the gas temperature at the same level of other X-ray quantities like luminosity. Our results on the X-ray and SZ scaling relations show a tension between the quantities more related to the global energy of the system (e.g. gas temperature, gravitating mass) and the indicators of the structure of the ICM (e.g. gas density profile, central Compton parameter y_0). Indeed, by using a robust fitting technique, the most significant deviations from the values of the slope predicted from the self-similar model are measured in the $L - T$, $L - M_{\text{tot}}$, $M_{\text{gas}} - T$, $y_0 - T$ relations. When the slope is fixed to the self-similar value, these relations consistently show a negative evolution suggesting a scenario in which the ICM at higher redshift has lower both X-ray luminosity and pressure in the central regions than the expectations from self-similar model. These effects are more evident in relaxed clusters in the redshift range 0.14–0.45, where a more defined core is present and the assumed hypotheses on the state of the ICM are more reliable.

Key words: galaxies: clusters: general – cosmic microwave background – cosmology: observations – X-ray: galaxies: clusters

1 INTRODUCTION

Clusters of galaxies represent the largest virialized structures in the present universe, formed at relatively late times. The hierarchical scenario provides a picture in which the primordial density fluctuations generate proto-structures which are then subject to gravitational collapse and mass accretion, producing larger and larger systems. The cosmic baryons fall into the gravitational potential of the cluster dark matter (DM) halo formed in this way, while the collapse and the subsequent shocks heat the intra-cluster medium (ICM) up to the virial temperature ($0.5 \lesssim T \lesssim 10$ keV).

In the simplest scenario which neglects all non-radiative processes, the gravity, which has not preferred scales, is the only re-

sponsible for the physical properties of galaxy clusters: for this reason they are expected to maintain similar properties when rescaled with respect to their mass and formation epoch. This allows to build a very simple model to relate the physical parameters of clusters: the so-called self-similar model (Kaiser 1986; Evrard & Henry 1991). Based on that, we can derive scaling relations (see Sect. 3) between X-ray quantities (like temperature T , mass M , entropy and luminosity L), and between X-ray and Sunyaev-Zel’dovich (SZ) measurements (like the Compton- y parameter), thanks to the assumption of spherical collapse for the DM halo and hydrostatic equilibrium of the gas within the DM gravitational potential. These relations provide a powerful test for the adiabatic scenario. In particular, in the recent years the studies about the X-ray scaling laws (see, e.g., Allen & Fabian 1998; Markevitch 1998; Ettori et al. 2004b; Arnaud et al. 2005; Vikhlinin et al. 2005;

* E-mail: andrea.morandi@studio.unibo.it

Kotov & Vikhlinin 2005), together with observations of the entropy distribution in galaxy clusters (see, e.g., Ponman et al. 1999, 2003) and the analysis of simulated systems including cooling and extra non-gravitational energy injection (see, e.g., Borgani et al. 2004) have suggested that the simple adiabatic scenario is not giving an appropriate description of galaxy clusters. In particular the most significant deviations with respect to the self-similar predictions are: (i) a lower (by $\sim 30 - 40$ per cent) normalization of the $M - T$ relation in real clusters with respect to adiabatic simulations (Evrard et al. 1996); (ii) steeper slopes for the $M - T$ and $L - T$ relations; (iii) an entropy ramp in the central regions of clusters (see, e.g., Ponman et al. 1999, 2003). These deviations are likely the evidence of non-radiative processes, like non-gravitational heating due to energy injection from supernovae, AGN, star formation or galactic winds (see, e.g., Pearce et al. 2001; Tozzi & Norman 2001; Bialek et al. 2001; Babul et al. 2002; Borgani et al. 2002; Brighenti & Mathews 2006) or cooling (see, e.g., Bryan 2000). More recently some authors pointed out that there is a mild dependence of the X-ray scaling relations on the redshift, suggesting that there should be an evolution of these non-gravitational processes with z (Ettori et al. 2004b).

An additional and independent method to evaluate the role of radiative processes is the study of the scaling relations based on the thermal SZ effect (Sunyaev & Zeldovich 1970), which offers a powerful tool for investigating the same physical properties of the ICM, being the electron component of cosmic baryons responsible of both the X-ray emission and the SZ effect. The advantage of the latter on the former is the possibility of exploring clusters at higher redshift, because of the absence of the cosmological dimming. Moreover, since the SZ intensity depends linearly on the density, unlike the X-ray flux, which depends on the squared density, with the SZ effect it is possible to obtain estimates of the physical quantities of the sources reducing the systematic errors originated by the presence of sub-clumps and gas in multi-phase state and to study in a complementary way to the X-ray analysis the effects of extra-physics on the collapse of baryons in cluster dark matter halos, both via numerical simulations (White et al. 2002; da Silva et al. 2004; Diaferio et al. 2005; Nagai 2006) and observationally (Cooray 1999; McCarthy et al. 2003a,b; Benson et al. 2004; LaRoque et al. 2006; Bonamente et al. 2006).

The main purpose of this paper is to understand how these SZ and X-ray scaling relations evolve with redshift. In particular we want to quantify how much they differ from the self-similar expectations in order to evaluate the amplitude of the effects of the non-gravitational processes on the physical properties of ICM. Another issue we want to debate is which relations can be considered a robust tool to link different cluster physical quantities: this has important consequences on the possibility of using clusters as probes for precision cosmology. To do that, we have assembled a sample of 24 galaxies clusters, for which measurements of the Compton- y parameter are present in the literature. Respect the previous works we have done our own spatially resolved X-ray analysis recovering X-ray and SZ quantity necessary to investigate scaling relations. We have performed a combined spatial and spectral analysis of the X-ray data, which allows us to derive the radial profile for temperature, pressure, and density in a robust way. These results, which have high spatial resolution, rely only on the hydrostatic equilibrium hypothesis and spherical geometry of the sources. Moreover we can compare the observed physical quantities with the results of hydrodynamical numerical simulations in a consistent way.

The paper is organized as follows. In Sect. 2 we introduce our cluster sample and we describe the method applied to determine

the X-ray properties (including the data reduction procedure) and the corresponding SZ quantities. In Sect. 3 we report our results about the scaling relations here considered, including the presentation of the adopted fitting procedure. Sect. 4 is devoted to a general discussion of our results, while in Sect. 5 we summarize our main conclusions. We leave to the appendices the discussion of some technical details of our data reduction procedure.

Hereafter we have assumed a flat Λ CDM cosmology, with matter density parameter $\Omega_{0m} = 0.3$, cosmological constant density parameter $\Omega_{\Lambda} = 0.7$, and Hubble constant $H_0 = 70$ km/s/Mpc. Unless otherwise stated, we estimated the errors at the 68.3 per cent confidence level.

2 THE DATASET

2.1 Data reduction

We have considered a sample of galaxy clusters for which we have SZ data from the literature and X-ray data from archives (see Tables 1 and 2, respectively). In particular, we have considered the original sample of McCarthy et al. (2003b), to which we added two more objects from the sample discussed by Benson et al. (2004). For all these clusters we have analyzed the X-ray data extracted from the *Chandra* archive. In total we have 24 galaxy clusters with redshift ranging between 0.14 and 0.82, emission-weighted temperature in the range 6-12 keV and X-ray luminosity between 10^{45} and 10^{46} erg s $^{-1}$. In the whole sample we have 11 cooling core clusters and 13 no-cooling core ones (hereafter CC and NCC clusters, respectively) defined according to the criterion that their cooling time in the inner regions is lower than the Hubble time at the cluster redshift.

We summarize here the most relevant aspects of the X-ray data reduction procedure. Most of the observations have been carried out using ACIS-I, while for 4 clusters (A1835, A370, MS0451.6-0305, MS1137.5+6625) we have data from the Back Illuminated S3 chip of ACIS-S. We have reprocessed the event 1 file retrieved from the *Chandra* archive with the CIAO software (version 3.2.2) distributed by the *Chandra* X-ray Observatory Centre. We have run the tool `acisss_proc_events` to apply corrections for charge transfer inefficiency (for the data at 153 K), re-computation of the events grade and flag background events associated with collisions on the detector of cosmic rays. We have considered the gain file provided within CALDB (version 3.0) in this tool for the data in FAINT and VFaint modes. Then we have filtered the data to include the standard events grades 0, 2, 3, 4 and 6 only, and therefore we have filtered for the Good Time Intervals (GTIs) supplied, which are contained in the `flt1.fits` file. We checked for unusual background rates through the script `analyze_ltcrv`, so we removed those points falling outside $\pm 3\sigma$ from the mean value. Finally, we have applied a filter to the energy (300-9500 keV) and CCDs, so as to obtain an events 2 file.

2.2 Spatial and spectral analysis

The images have been extracted from the events 2 files in the energy range (0.5-5.0 keV), corrected by using the exposure map to remove the vignetting effects, by masking out the point sources. So as to determine the centroid (x_c, y_c) of the surface brightness we have fitted the images with a circular one-dimensional (1D) isothermal β -model (Cavaliere & Fusco-Femiano 1976), by adding a constant brightness model, and leaving x_c and y_c free as parameters in

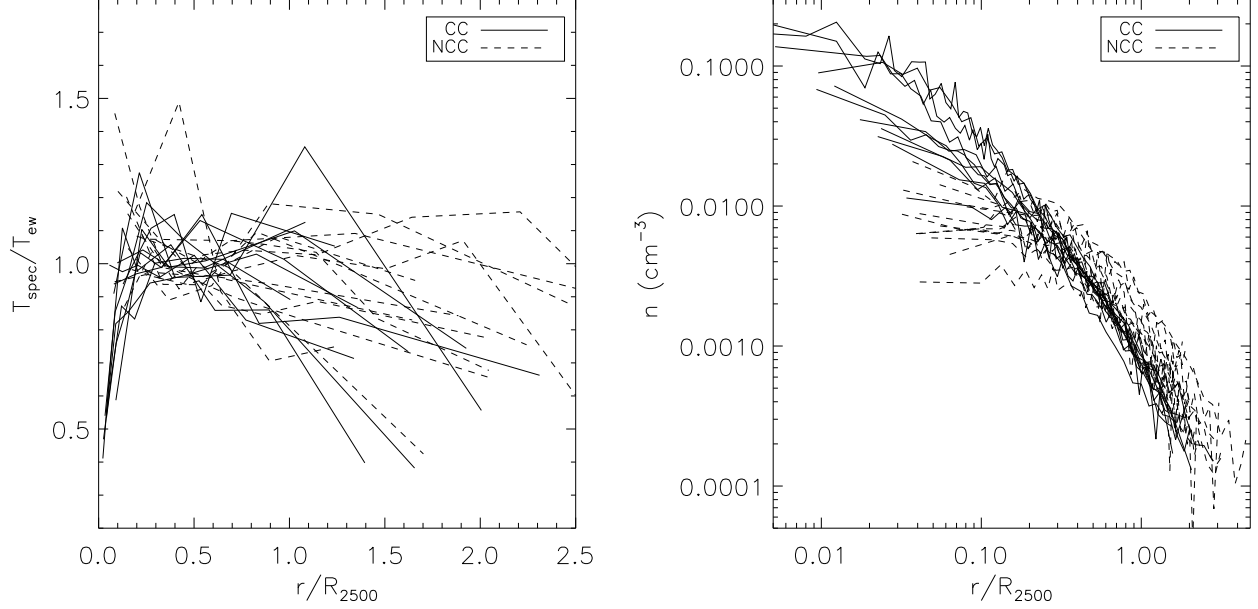


Figure 1. The radial profiles for the projected temperature T_{spec} , normalized using the cooling-core corrected temperature T_{ew} , and for density are shown for all objects of our sample in the left and right panels, respectively. Solid and dashed lines refer to clusters with or without a central cooling flow, respectively

the best fit. We constructed a set of n ($n \sim 15 - 40$) circular annuli around the centroid of the surface brightness up to a maximum distance R_{spat} (also reported in Table 2), selecting the radii according to the following criteria: the number of net counts of photons from the source in the (0.5-5.0 keV) band is at least 200-1000 per annulus and the signal-to-noise ratio is always larger than 2. The background counts have been estimated from regions of the same exposure which are free from source emissions.

The spectral analysis has been performed by extracting the source spectra from n^* ($n^* \sim 3 - 8$) circular annuli of radius r_m around the centroid of the surface brightness. We have selected the radius of each annulus out to a maximum distance R_{spec} (reported in Table 2), according to the following criteria: the number of net counts of photons from the source in the band used for the spectral analysis is at least 2000 per annulus and corresponds to a fraction of the total counts always larger than 30 per cent.

The background spectra have been extracted from regions of the same exposure in the case of the ACIS-I data, for which we always have some areas free from source emission. Conversely, for the ACIS-S data we have considered the ACIS-S3 chip only and we have equally used the local background, but we have checked for systematic errors due to possible source contamination of the background regions. This is done considering also the ACIS “blank-sky” background files, which we have re-processed if their gain file does not match the one of the events 2 file; then we have applied the aspect solution files of the observation to the background dataset by using `reproject_events`, so as to estimate the background for our data. We have verified that the spectra produced by the two methods are in good agreement, and at last we decided to show only the results obtained using the local background.

All the point sources has been masked out by visual inspection. Then we have calculated the redistribution matrix files (RMF) and the ancillary response files (ARF) for each annulus: in particular we have used the tools `mkacisrmf` and `mkrmf` (for the data

at 120 K and at 110 K, respectively) to calculate the RMF, and the tool `mkarf` to derive the ARF of the regions.

For each of the n^* annuli the spectra have been analyzed by using the package XSPEC (Arnaud 1996) after grouping the photons into bins of 20 counts per energy channel (using the task `grppha` from the FTOOLS software package) and applying the χ^2 -statistics. The spectra are fitted with a single-temperature absorbed MEKAL model (Kaastra 1992; Liedahl et al. 1995) multiplied by a positive absorption edge as described in Vikhlinin et al. (2005): this procedure takes into account a correction to the effective area consisting in a 10 per cent decrement above 2.07 keV. The fit is performed in the energy range 0.6-7 keV (0.6-5 keV for the outermost annulus only) by fixing the redshift to the value obtained from optical spectroscopy and the absorbing equivalent hydrogen column density N_{H} to the value of the Galactic neutral hydrogen absorption derived from radio data (Dickey & Lockman 1990), except for A520, A697, A2163, MS1137.5+6625, MS1358.4+6245 and A2390, where we have decided to leave N_{H} free due to the inconsistency between the tabulated radio data and the spectral fit result. Apart for these objects where also the Galactic absorption is left free, we consider three free parameters in the spectral analysis for m -th annulus: the normalization of the thermal spectrum $K_m \propto \int n_e^2 dV$, the emission-weighted temperature $T_{\text{proj},m}^*$; the metallicity Z_m retrieved by employing the solar abundance ratios from Anders & Grevesse (1989). The best-fit spectral parameters are listed in Table 2.

The total (cooling-core corrected) temperature T_{ew} has been extracted in a circular region of radius R , with $100 \text{ kpc} < R < R_{\text{spec}}$, centred on the symmetrical centre of the brightness distribution. In the left panel of Fig. 1 we present for all clusters of our sample the projected temperature profile (T_{spec}) normalized by T_{ew} as a function of the distance from the centre R , given in units of R_{2500} , where R_{2500} is the radius corresponding to an overdensity of 2500.

Table 2. The X-ray properties of the galaxy clusters in our sample. For each object different columns report the name, the redshift z , the identification number of the *Chandra* observation, the used ACIS mode, the exposure time t_{exp} , the neutral hydrogen absorption N_{H} (the labels f and t refer to objects for which N_{H} has been fixed to the Galactic value or thawed, respectively), the physical scale corresponding to 1 arcmin, the maximum radii used for the spatial and for the spectral analysis (R_{spat} and R_{spec} , respectively), the emission-weighted temperature T_{ew} , the metallicity Z (in solar units), a flag for the presence or not of a cooling core (labeled CC and NCC, respectively), the mass-weighted temperature T_{mw} , the gas mass M_{gas} , and the bolometric X-ray luminosity L . The last three columns refer to an overdensity of 2500. Sources extracted from the McCarthy et al. (2003b) sample and from the Benson et al. (2004) sample are indicated by apices (1) and (2), respectively.

name	z	obs.	ACIS mode	t_{exp} (ks)	N_{H} (10^{20}cm^{-2})	1' scale (kpc)	R_{spat} (kpc)	R_{spec} (kpc)	T_{ew} (keV)	Z (Z_{\odot})	CC/ NCC	T_{mw} (keV)	M_{gas} ($10^{13} M_{\odot}$)	L (10^{45}erg/s)
A1413 ⁽¹⁾	0.143	1661	I	9.7	2.2(f)	151	1111	1359	$6.25^{+0.36}_{-0.33}$	$0.45^{+0.11}_{-0.10}$	CC	6.58 ± 0.42	2.87 ± 0.09	1.28 ± 0.03
A2204 ⁽¹⁾	0.152	6104	I	9.6	5.7(f)	159	1183	1262	$9.18^{+0.75}_{-0.65}$	$0.49^{+0.14}_{-0.13}$	CC	10.52 ± 0.62	5.64 ± 0.18	4.21 ± 0.14
A1914 ⁽¹⁾	0.171	3593	I	18.8	0.9(f)	175	1449	1576	$8.93^{+0.48}_{-0.45}$	$0.23^{+0.07}_{-0.07}$	NCC	8.90 ± 0.43	3.94 ± 0.09	1.88 ± 0.05
A2218 ⁽¹⁾	0.176	1666	I	36.1	3.2(f)	179	1231	1320	$6.88^{+0.33}_{-0.30}$	$0.27^{+0.06}_{-0.06}$	NCC	6.67 ± 0.24	2.42 ± 0.07	0.84 ± 0.02
A665 ⁽¹⁾	0.182	3586	I	29.1	4.2(f)	184	1589	1476	$7.14^{+0.33}_{-0.31}$	$0.28^{+0.06}_{-0.06}$	NCC	7.02 ± 0.20	2.61 ± 0.08	1.22 ± 0.03
A1689 ⁽¹⁾	0.183	1663	I	10.6	1.8(f)	185	1446	1059	$8.72^{+0.63}_{-0.56}$	$0.23^{+0.10}_{-0.10}$	CC	6.97 ± 1.19	5.24 ± 0.14	3.15 ± 0.09
A520 ⁽¹⁾	0.199	4215	I	66.2	3.5(t)	197	1327	1455	$8.24^{+0.31}_{-0.28}$	$0.32^{+0.05}_{-0.05}$	NCC	9.70 ± 0.55	3.47 ± 0.09	0.92 ± 0.02
A2163 ⁽¹⁾	0.203	1653	I	71.1	17.5(t)	200	1846	1807	$12.00^{+0.28}_{-0.26}$	$0.24^{+0.03}_{-0.03}$	NCC	11.70 ± 0.41	6.71 ± 0.07	4.80 ± 0.05
A773 ⁽¹⁾	0.217	5006	I	19.8	1.4(f)	211	1105	1384	$7.23^{+0.62}_{-0.52}$	$0.37^{+0.12}_{-0.12}$	NCC	7.09 ± 0.36	2.34 ± 0.11	1.13 ± 0.04
A2261 ⁽¹⁾	0.224	5007	I	24.3	3.3(f)	216	1588	1595	$7.47^{+0.47}_{-0.47}$	$0.37^{+0.10}_{-0.10}$	CC	7.56 ± 0.38	3.28 ± 0.08	2.02 ± 0.07
A2390 ⁽²⁾	0.232	4193	S	92.0	8.3(t)	222	1205	873	$10.18^{+0.23}_{-0.21}$	$0.29^{+0.03}_{-0.03}$	CC	10.02 ± 0.16	6.98 ± 0.08	4.66 ± 0.05
A1835 ⁽¹⁾	0.253	495	S	10.3	2.3(f)	237	914	970	$8.62^{+0.60}_{-0.54}$	$0.44^{+0.12}_{-0.12}$	CC	8.75 ± 0.80	5.89 ± 0.60	5.58 ± 0.22
A697 ⁽¹⁾	0.282	4217	I	19.5	1.0(t)	256	1865	1679	$10.21^{+0.83}_{-0.75}$	$0.36^{+0.11}_{-0.11}$	NCC	9.89 ± 0.67	4.21 ± 0.21	2.52 ± 0.09
A611 ⁽¹⁾	0.288	3194	S	35.1	5.0(f)	260	969	1172	$6.06^{+0.38}_{-0.34}$	$0.31^{+0.09}_{-0.08}$	CC	6.32 ± 0.37	2.46 ± 0.07	1.25 ± 0.03
Zw3146 ⁽¹⁾	0.291	909	I	46.0	3.0(f)	262	1061	1287	$7.35^{+0.27}_{-0.26}$	$0.26^{+0.05}_{-0.05}$	CC	8.48 ± 0.30	5.56 ± 0.15	4.32 ± 0.11
A1995 ⁽¹⁾	0.319	906	S	44.5	1.4(f)	279	877	914	$7.56^{+0.45}_{-0.41}$	$0.38^{+0.09}_{-0.09}$	CC	7.75 ± 0.48	3.39 ± 0.11	1.51 ± 0.05
MS1358.4+6245 ⁽¹⁾	0.327	516	S	34.1	3.2(t)	283	796	813	$7.51^{+0.70}_{-0.61}$	$0.38^{+0.15}_{-0.14}$	CC	8.05 ± 0.58	2.98 ± 0.15	1.37 ± 0.06
A370 ⁽¹⁾	0.375	515	S	48.6	3.1(f)	310	926	762	$7.37^{+0.58}_{-0.53}$	$0.28^{+0.10}_{-0.10}$	NCC	7.73 ± 0.41	3.35 ± 0.14	1.11 ± 0.04
RXJ2228+2037 ⁽¹⁾	0.421	3285	I	19.8	4.9(f)	332	1320	1636	$6.86^{+0.89}_{-0.71}$	$0.35^{+0.15}_{-0.15}$	NCC	7.48 ± 0.81	2.36 ± 0.15	1.64 ± 0.08
RXJ1347.5-1145 ⁽¹⁾	0.451	3592	I	57.7	4.9(f)	346	1558	1560	$13.92^{+1.14}_{-0.93}$	$0.19^{+0.08}_{-0.09}$	CC	15.32 ± 0.83	8.99 ± 0.19	8.84 ± 0.38
MS0015.9+1609 ⁽¹⁾	0.546	520	I	67.4	4.1(f)	383	1889	849	$8.29^{+0.49}_{-0.43}$	$0.32^{+0.06}_{-0.06}$	NCC	8.00 ± 0.37	3.13 ± 0.09	2.46 ± 0.06
MS0451.6-0305 ⁽¹⁾	0.550	902	S	41.1	5.1(f)	385	1092	1325	$9.09^{+0.70}_{-0.61}$	$0.29^{+0.10}_{-0.09}$	NCC	8.99 ± 1.15	6.21 ± 0.72	3.92 ± 0.12
MS1137.5+6625 ⁽¹⁾	0.784	536	I	116.4	3.5(t)	447	706	880	$5.48^{+0.89}_{-0.71}$	$0.25^{+0.25}_{-0.22}$	NCC	6.28 ± 0.57	1.73 ± 0.10	1.00 ± 0.06
EMSS1054.5-0321 ⁽²⁾	0.823	512	S	71.1	3.6(f)	455	763	895	$9.00^{+1.39}_{-1.10}$	$0.25^{+0.17}_{-0.17}$	NCC	9.38 ± 1.31	2.55 ± 0.18	1.35 ± 0.13

2.3 Spectral deprojection analysis

To measure the pressure and gravitating mass profiles in our clusters, we deproject the projected physical properties obtained with the spectral analysis by using an updated and extended version of the technique presented in Ettori et al. (2002) and discussed in full detail in Appendix A. Here we summarize briefly the main characteristics of the adopted technique: (i) the electron density $n_e(r)$ is recovered both by deprojecting the surface brightness profile and the spatially resolved spectral analysis obtaining a few tens of radial measurements; (ii) once a functional form of the DM density profile $\rho = \rho(r, \mathbf{q})$, where $\mathbf{q} = (q_1, q_2, \dots, q_h)$ are free parameters of the DM analytical model, and the gas pressure P_0 at R_{spec} are assumed, the deprojected gas temperature, $T(\mathbf{q}, P_0)$, is obtained by integration of the hydrostatic equilibrium equation:

$$P(r, \mathbf{q}, P_0) = P_0 - \int_{R_{\text{spec}}}^r n_{\text{gas}}(s) \mu m_H \frac{G M(\mathbf{q}, s)}{s^2} ds, \quad (1)$$

where $\mu = 0.6$ is the average molecular weight, m_H is the proton mass. So $T(\mathbf{q}, P_0) = P(\mathbf{q}, P_0)/n_{\text{gas}}$ expressed in keV units. In the present study, to parametrize the cluster mass distribution, we consider two models: the universal density profile proposed by

Navarro et al. (1997) (hereafter NFW) and the one suggested by Rasia et al. (2004) (hereafter RTM).

The NFW profile is given by

$$\rho(x) = \frac{\rho_{c,z} \delta_{c,\text{NFW}}}{(x/x_s)(1+x/x_s)^2}, \quad (2)$$

where $\rho_{c,z} \equiv 3H(z)^2/8\pi G$ is the critical density of the universe at redshift z , $H_z \equiv E_z H_0$, $E_z = [\Omega_M(1+z)^3 + (1-\Omega_M-\Omega_\Lambda)(1+z)^2 + \Omega_\Lambda]^{1/2}$, and

$$\delta_{c,\text{NFW}} = \frac{\Delta}{3 \ln(1+c) - c/(1+c)}, \quad (3)$$

where $c \equiv r_{\text{vir}}/r_s$ is the concentration parameter, r_s is the scale radius, $x \equiv r/r_{\text{vir}}$, $x_s \equiv r_s/r_{\text{vir}}$.

The RTM mass profile is given by:

$$\rho(x) = \frac{\rho_{c,z} \delta_{c,\text{RTM}}}{x(x+x_s^*)^{3/2}}, \quad (4)$$

with $x_s^* \equiv r_s^*/r_{\text{vir}}$, where r_s^* is a reference radius and $\delta_{c,\text{RTM}}$ is given by:

$$\delta_{c,\text{RTM}} \equiv \frac{\Delta}{6 [(1+2x_s^*)/(1+x_s^*)^{1/2} - 2x_s^{*1/2}]}. \quad (5)$$

Table 1. The SZ parameters for the galaxy clusters in our sample. For each object different columns report the name, the central value (y_0) of the Compton y -parameter, the SZ flux integrated up to an overdensity of 2500 and over a fixed solid angle $\Omega = 1$ arcmin (y_{2500} and y_Ω , respectively) divided by the function $g(x)$ (see eq. 9), and the parameter η (see text). For two objects (namely A1914 and RXJ2228+2037) the corresponding errors are not provided by McCarthy et al. (2003b): in the following analysis we will assume for them a formal 1σ error of 20 per cent.

name	y_0 ($\times 10^4$)	y_{2500} (mJy)	y_Ω (mJy)	η
A1413	$1.61^{+0.20}_{-0.22}$	40.3 ± 5.2	7.67 ± 1.00	0.99
A2204	$1.80^{+0.46}_{-0.62}$	53.1 ± 16.0	7.91 ± 2.38	0.79
A1914	1.59	26.2 ± 5.2	6.41 ± 1.28	1.20
A2218	$1.37^{+0.18}_{-0.26}$	25.7 ± 4.1	6.62 ± 1.04	1.03
A665	$1.37^{+0.26}_{-0.31}$	37.1 ± 7.7	8.12 ± 1.69	0.92
A1689	$3.24^{+0.22}_{-0.20}$	56.8 ± 3.7	13.34 ± 0.86	0.94
A520	$1.24^{+0.17}_{-0.19}$	38.8 ± 5.6	7.53 ± 1.08	1.10
A2163	$3.56^{+0.25}_{-0.27}$	142.6 ± 10.5	22.69 ± 1.67	0.74
A773	$2.37^{+0.28}_{-0.32}$	34.8 ± 4.4	10.99 ± 1.41	0.95
A2261	$3.18^{+0.35}_{-0.40}$	39.5 ± 4.6	12.40 ± 1.46	0.92
A2390	$3.57^{+0.42}_{-0.42}$	78.4 ± 9.2	17.39 ± 2.05	0.75
A1835	$4.70^{+0.31}_{-0.29}$	48.3 ± 3.1	16.44 ± 1.06	0.80
A697	$2.65^{+0.32}_{-0.32}$	44.1 ± 5.3	13.88 ± 1.66	0.96
A611	$1.60^{+0.24}_{-0.24}$	11.2 ± 1.7	5.39 ± 0.82	1.02
Zw3146	$1.61^{+0.25}_{-0.29}$	15.8 ± 2.6	5.67 ± 0.93	0.92
A1995	$1.92^{+0.14}_{-0.16}$	18.6 ± 1.5	8.22 ± 0.65	1.06
MS1358.4+6245	$1.47^{+0.16}_{-0.18}$	13.4 ± 1.5	5.87 ± 0.68	0.75
A370	$2.36^{+0.84}_{-0.45}$	18.9 ± 5.2	10.42 ± 2.84	1.19
RXJ2228+2037	2.40	14.9 ± 3.0	10.76 ± 2.15	0.88
RXJ1347.5-1145	$7.41^{+0.63}_{-0.68}$	44.4 ± 3.9	19.60 ± 1.74	0.70
MS0015.9+1609	$2.33^{+0.19}_{-0.20}$	11.5 ± 1.0	10.55 ± 0.89	0.97
MS0451.6-0305	$2.69^{+0.17}_{-0.19}$	12.5 ± 0.8	9.04 ± 0.60	1.31
MS1137.5+6625	$1.53^{+0.17}_{-0.19}$	2.4 ± 0.3	2.73 ± 0.32	1.16
EMSS1054.5-0321	$3.87^{+1.19}_{-1.12}$	11.8 ± 3.5	13.93 ± 4.16	1.04

So we have $\mathbf{q} = (c, r_s)$ and $\mathbf{q} = (x_s, r_{200})$ for the NFW and RTM models, respectively.

The comparison of the observed projected temperature profile $T_{\text{proj},m}^*$ (Sect. 2.2) with the deprojected $T(\mathbf{q}, P_0)$ (eq. A7 in Appendix A), once the latter has been re-projected by correcting for the temperature gradient along the line of sight as suggested in Mazzotta et al. (2004), provides the best estimate of the free parameters (\mathbf{q}, P_0) through a χ^2 minimization, and therefore of $T(\mathbf{q}, P_0)$ (see an example in Figure 2).

In the right panel of Fig. 1 we present the density profiles (plotted versus r/R_{2500}) as determined through the previous method. In general, we find there is no significant effect on the determination of the physical parameters when adopting the two different DM models. Hereafter we will use the physical parameters determined using the RTM model, reported with their corresponding errors in Table 2, where we also list the exposure time, the number and the instrument (ACIS-I or ACIS-S) used for each of the *Chandra* observations.

Finally we computed the total mass enclosed in a sphere of radius R_Δ as $M(\mathbf{q})(< R_\Delta) = \int_0^{R_\Delta} \rho(r, \mathbf{q}) dV$ where the radius R_Δ corresponds to a given overdensity Δ : we considered the cases where the overdensity is equal to 2500 and 500. The values for masses and radii, together with the parameters (\mathbf{q}, P_0) for the RTM model, are reported in Table 3. The errors on the different

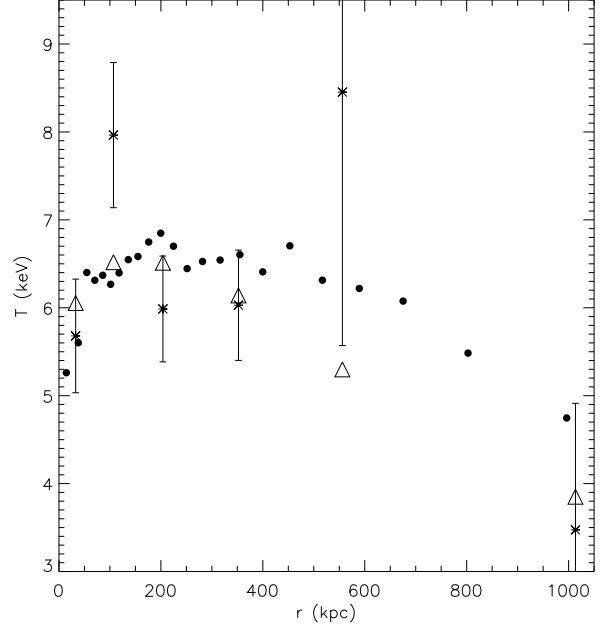


Figure 2. Example of temperature spectral deprojection for cluster A1413. We display the two quantities which enter in the eq. A7 in the spectral deprojection analysis to retrieve the physical parameters: the observed spectral projected temperature $T_{\text{proj},m}^*$ (stars with errorbars) and the theoretical projected temperature (triangles, indicated as $T_{\text{proj},m}$ in Appendix A). We also show the theoretical deprojected temperature $T(\mathbf{q}, P_0)$ (points), which generates $T_{\text{proj},m}$ through convenient projection techniques.

quantities represent the 68.3 per cent confidence level and are computed by looking to the regions in the parameter space where the reduction of χ^2 with respect to its minimum value χ_{min}^2 is smaller than a given threshold, fixed according to the number of degrees of freedom d.o.f. (see, e.g., Press et al. 1992). Notice that we included in the eq.(1) the statistical errors related to measurement errors of $n_{\text{gas}}(r)$.

2.4 Determination of the X-ray properties

The bolometric X-ray luminosity $L(< R_\Delta)$ has been calculated by correcting the observed luminosity $L(100 \text{ kpc} < r < R_{\text{spec}})$ determined from the spectral analysis performed by XSPEC excluding the central cooling region of 100 kpc (the results are reported in Table 2):

$$L(< R_\Delta) = L(100 \text{ kpc} < r < R_{\text{spec}}) \frac{\int_0^{x_\Delta} (1+x^2)^{-3\beta} x^2 dx}{K_{\text{corr}}}, \quad (6)$$

where $x = r/r_c$, $x_\Delta = R_\Delta/r_c$, r_c and β are the best-fit parameters of the β -model on the image brightness, K_{corr} is the normalization of the thermal spectrum drawn with XSPEC, and corrected for the emission from the spherical source up to 10 Mpc intercepted by the line of sight: $K_{\text{corr}} = \int_{x_0}^{x_1} (1+x^2)^{-3\beta} x^2 dx + \int_{x_1}^{x_2} (1+x^2)^{-3\beta} x^2 (1 - \cos \theta) dx - \int_{x_0}^{x_2} (1+x^2)^{-3\beta} x^2 (1 - \cos \theta^*) dx$, with $\theta = \arcsin(x_1/x)$, $\theta^* = \arcsin(x_0/x)$, $x_0 = 100 \text{ kpc}/r_c$, $x_1 = R_{\text{spec}}/r_c$ and $x_2 = 10 \text{ Mpc}/r_c$.

The gas mass M_{gas} enclosed in a circular region having overdensity Δ has been computed from the total gas density $n_{\text{gas},j}$, that we directly obtained from the spectral deprojection, up to R_{spec} .

Table 3. Different physical properties for the clusters in our sample. For each object the different columns report the name, the minimum value for χ^2 (with the corresponding number of degrees of freedom d.o.f.), the virial radius r_{vir} , the reference scale x_s , the value of the pressure P_0 , the mass and the radius corresponding to an overdensity of 2500 (M_{2500} and R_{2500} , respectively), the mass and the radius corresponding to an overdensity of 500 (M_{500} and R_{500} , respectively). All quantities are derived by assuming the RTM model.

name	$\chi^2_{\text{min}}(\text{d.o.f.})$	r_{vir} (kpc)	x_s	P_0 ($10^{-12} \text{ erg cm}^{-3}$)	M_{2500} ($10^{14} M_{\odot}$)	R_{2500} (kpc)	M_{500} ($10^{14} M_{\odot}$)	R_{500} (kpc)
A1413	5.29(3)	1853 ± 255	0.11 ± 0.05	1.87 ± 0.48	$2.30(\pm 0.46)$	$520(\pm 57)$	$5.58(\pm 2.25)$	$1195(\pm 232)$
A2204	4.24(5)	2840 ± 357	0.16 ± 0.03	0.73 ± 0.71	$6.74(\pm 1.40)$	$742(\pm 91)$	$19.12(\pm 6.68)$	$1796(\pm 320)$
A1914	2.29(5)	1809 ± 202	0.03 ± 0.03	1.98 ± 0.64	$3.39(\pm 0.76)$	$586(\pm 61)$	$5.99(\pm 2.28)$	$1212(\pm 202)$
A2218	0.61(2)	1653 ± 180	0.06 ± 0.04	1.53 ± 0.33	$2.14(\pm 0.30)$	$502(\pm 36)$	$4.36(\pm 1.33)$	$1088(\pm 152)$
A665	1.23(5)	2177 ± 359	0.31 ± 0.16	1.72 ± 0.44	$1.88(\pm 0.16)$	$480(\pm 30)$	$7.77(\pm 2.71)$	$1317(\pm 260)$
A1689	0.68(4)	2159 ± 323	0.09 ± 0.04	1.24 ± 1.05	$4.14(\pm 0.95)$	$624(\pm 76)$	$9.40(\pm 3.65)$	$1402(\pm 260)$
A520	0.08(3)	2487 ± 1340	0.23 ± 0.74	1.58 ± 0.57	$3.72(\pm 0.93)$	$599(\pm 102)$	$12.66(\pm 8.50)$	$1540(\pm 546)$
A2163	3.00(5)	4884 ± 637	1.46 ± 0.46	1.44 ± 0.26	$4.07(\pm 0.69)$	$616(\pm 102)$	$52.58(\pm 10.72)$	$2472(\pm 396)$
A773	1.38(2)	1672 ± 486	0.09 ± 0.14	2.90 ± 0.51	$2.01(\pm 0.45)$	$485(\pm 60)$	$4.54(\pm 3.49)$	$1087(\pm 388)$
A2261	2.82(3)	1851 ± 191	0.10 ± 0.03	0.87 ± 0.46	$2.68(\pm 0.44)$	$532(\pm 46)$	$6.17(\pm 1.79)$	$1201(\pm 168)$
A2390	23.08(4)	3557 ± 497	0.41 ± 0.11	2.66 ± 0.81	$6.59(\pm 0.64)$	$716(\pm 52)$	$33.22(\pm 9.88)$	$2099(\pm 373)$
A1835	0.80(1)	2259 ± 413	0.14 ± 0.05	5.92 ± 1.70	$4.09(\pm 1.34)$	$606(\pm 113)$	$10.95(\pm 6.39)$	$1439(\pm 414)$
A697	1.17(4)	2251 ± 1491	0.21 ± 0.72	2.69 ± 2.77	$3.23(\pm 0.88)$	$554(\pm 94)$	$10.46(\pm 8.47)$	$1402(\pm 588)$
A611	0.81(3)	1719 ± 242	0.12 ± 0.05	2.14 ± 0.59	$2.11(\pm 0.45)$	$480(\pm 56)$	$5.18(\pm 2.15)$	$1107(\pm 222)$
Zw3146	4.36(3)	2984 ± 403	0.31 ± 0.07	1.26 ± 0.86	$5.41(\pm 0.81)$	$656(\pm 68)$	$22.50(\pm 7.58)$	$1804(\pm 344)$
A1995	3.05(2)	2585 ± 2042	0.32 ± 0.67	3.41 ± 2.84	$3.51(\pm 1.32)$	$562(\pm 149)$	$14.96(\pm 13.96)$	$1558(\pm 804)$
MS1358.4+6245	0.60(1)	2748 ± 2134	0.38 ± 0.66	3.67 ± 3.11	$3.62(\pm 1.64)$	$566(\pm 184)$	$17.37(\pm 16.70)$	$1633(\pm 885)$
A370	4.21(1)	2195 ± 822	0.23 ± 0.33	0.06 ± 1.44	$3.10(\pm 0.74)$	$528(\pm 82)$	$10.58(\pm 7.70)$	$1359(\pm 518)$
RXJ2228+2037	0.12(2)	1648 ± 1164	0.19 ± 0.73	3.11 ± 1.72	$1.59(\pm 0.46)$	$415(\pm 90)$	$4.90(\pm 4.35)$	$1033(\pm 464)$
RXJ1347.5-1145	3.58(5)	2703 ± 187	0.13 ± 0.02	0.01 ± 0.15	$9.49(\pm 1.26)$	$744(\pm 56)$	$24.00(\pm 4.75)$	$1734(\pm 170)$
MS0015.9+1609	0.96(4)	2129 ± 433	0.48 ± 0.39	0.24 ± 0.55	$1.72(\pm 0.25)$	$406(\pm 50)$	$9.75(\pm 2.82)$	$1237(\pm 224)$
MS0451.6-0305	0.14(5)	2118 ± 1915	0.21 ± 0.73	3.63 ± 3.24	$3.68(\pm 1.43)$	$522(\pm 130)$	$11.89(\pm 12.85)$	$1320(\pm 725)$
MS1137.5+6625	2.12(1)	1468 ± 284	0.17 ± 0.13	0.13 ± 0.47	$1.91(\pm 0.48)$	$382(\pm 58)$	$5.47(\pm 2.79)$	$928(\pm 238)$
EMSS1054.5-0321	0.03(1)	3060 ± 1666	1.39 ± 0.75	5.58 ± 7.61	$2.17(\pm 1.26)$	$393(\pm 168)$	$27.21(\pm 21.81)$	$1560(\pm 930)$

We have checked that the exclusion of the central cooling region does not significantly affect the resulting values for M_{gas} .

Finally we have estimated the total mass-weighted temperature:

$$T_{\text{mw}} \equiv \left(\sum_{i=1}^p T_j(\mathbf{q}, P_0) m_i \right) / \sum_{i=1}^p m_i \quad (7)$$

which can be compared to the total emission-weighted temperature T_{ew} ; p represents the number of annuli inside R_{2500} . Notice that our average deprojected temperature profile implies the following relation between the maximum, the deprojected and the mass-weighted temperatures: $T_{\text{max}} : T_{\text{ew}} : T_{\text{mw}} = 1 : 0.67 : 0.69$ ($1 : 0.83 : 0.88$ for the CC-only subsample). The physical parameters obtained in this way are also listed in Table 2 for all clusters of our sample.

2.5 Determination of the Sunyaev-Zel'dovich properties

The thermal SZ (Sunyaev & Zeldovich 1970) effect is a very small distortion of the spectrum of the cosmic microwave background (CMB), due to the inverse Compton scatter between cold CMB photons and hot ICM electrons (for recent reviews see, e.g., Birkinshaw 1999; Carlstrom et al. 2002; Rephaeli et al. 2005). This comptonization process statistically rises the photon energy, producing a distortion of the CMB black-body spectrum. The final result is a decrease (increase) of the CMB flux at frequencies smaller (larger) than about 218 GHz. The amplitude of this effect is directly proportional to the Compton parameter $y(\theta)$, which is defined as

$$y(\theta) = \frac{\sigma_T}{m_e c^2} \int P_e(\mathbf{r}) dl, \quad (8)$$

where θ is the angular distance from the cluster centre, σ_T is the Thomson cross-section, and $P_e(\mathbf{r}) \equiv n_e(\mathbf{r}) k T_e(\mathbf{r})$ is the pressure of the ICM electrons at the position \mathbf{r} ; the integral is done along the line of sight.

The SZ effect can be expressed as a change in the brightness:

$$\Delta I_{\text{SZ}} = g_{(x, T_e)} I_0 y, \quad (9)$$

respectively; here $I_0 \equiv 2(k T_{\text{CMB}})^3 / (hc)^2$, $x \equiv h\nu / k T_{\text{CMB}}$, T_{CMB} is the present CMB temperature and the function $g_{(x, T_e)}$ is given by:

$$g_{(x, T_e)} = \frac{x^4 e^x}{(e^x - 1)^2} \left(x \frac{e^x + 1}{e^x - 1} - 4 \right) (1 + o(x, T_e)), \quad (10)$$

and accounts for the frequency dependence of the SZ effect; the term $o(x, T_e)$ represents the relativistic correction (see, e.g., Itoh et al. 1998), which, however, is negligible for clusters having $T \lesssim 10$ keV.

We consider the Compton- y parameter integrated over the entire solid angle (and given in flux units) y_{Δ} defined as:

$$y_{\Delta} = I_0 \int_0^{\theta_{\Delta}} y(\theta) d\Omega; \quad (11)$$

To remove the dependence of y_{Δ} on the angular diameter distance $d_a(z)$ we use the intrinsic integrated Compton parameter Y , defined as:

$$Y \equiv d_a^2(z) y_{\Delta}. \quad (12)$$

The same quantity, but integrated over a fixed solid angle Ω , can be similarly written as:

$$y_\Omega = I_0 \int_0^\Omega y(\theta) d\Omega. \quad (13)$$

We fixed $\Omega = 1$ arcmin, that is \lesssim than the field of view of OVRO, used in the observations of most of the sources in our sample (see, e.g., McCarthy et al. 2003a). Notice that in order to remove the frequency dependence we have normalized Y , y_Δ and y_Ω to $g_{(x, T_e)}$.

To integrate eqs. (11) and (13) we have recovered $y(\theta)$ from eq. 8 by using the pressure profile $P(\mathbf{q}, P_0)$ determined in the spectral analysis (Sect. 2.3), renormalized in such a way that $y(0)$ equals the central Compton parameter y_0 taken from the literature. This method can lead to systematics on y_Ω and Y due to the fact that, even if we are assuming the true pressure profiles $P(r)$ in eq. (8), y_0 has been obtained by assuming an isothermal β -model inferred from the brightness profile. The value of y_0 is thus potentially dependent on the underlying model of $P(r)$. As discussed in recent works (see, e.g., LaRoque et al. 2006; Bonamente et al. 2006), the relaxation of the isothermal assumption should apply to the analysis of both X-ray and SZ data, to obtain a robust and consistent description of the physics acting inside galaxy clusters. Unfortunately, we have only the central Compton parameter, and not the complete uv -data, which are not public available: so it is very difficult to quantify the amplitude of this systematics, being y_0 determined through a best fit in the uv -plane.

Nevertheless, we can give an estimate in this way: we have computed the central Compton parameter $y_{0,X}^I$ inferred from the X-ray data by parametrizing first $P(r)$ in eq. (8) with a β -model inferred on the brightness images:

$$y_0 = \frac{\sigma T}{m_e c^2} n_0 k T_{\text{gas}} \int dx (1+x^2)^{(1-3\beta)/2} \quad (14)$$

with $n_0 = n_{\text{gas}}(r=0)$ derived from the brightness profile $B(r)$:

$$B(r=0) = \frac{1}{4\pi(1+z)^4} r_c \Lambda 0.82 n_0^2 \int dx (1+x^2)^{1/2-3\beta} \quad (15)$$

where Λ is the X-ray cooling function of the ICM in the cluster rest frame in cgs units ($\text{erg cm}^3 \text{s}^{-1}$) integrated over the energy range of the brightness images (0.5–5 keV). Then we have calculated $y_{0,X}^{II}$ by accounting in eq. 8 for the true pressure profile $P(\mathbf{q}, P_0)$ recovered by the spectral deprojection analysis (Sect. 2.3), and therefore we determined the ratio $\eta = y_{0,X}^{II}/y_{0,X}^I$. We notice that the parameter η differs from the unity of $\lesssim 25$ per cent, comparable to statistical errors.

The different quantities related to the SZ effect are listed in Table 1 for all clusters in our sample.

3 THE X-RAY AND SZ SCALING RELATIONS: THEORY AND FITTING PROCEDURE

3.1 The scaling relations in the self-similar model

The self-similar model (see, e.g., Kaiser 1986) gives a simple picture of the process of cluster formation in which the ICM physics is driven by the infall of cosmic baryons into the gravitational potential of the cluster DM halo. The collapse and subsequent shocks heat the ICM up to the virial temperature. Thanks to this model, which assumes that gravity is the only responsible for the observed values of the different physical properties of galaxy clusters, we have a simple way to establish theoretical analytic relations between them.

Numerical simulations confirm that the DM component in clusters of galaxies, which represents the dominant fraction of the mass, has a remarkably self-similar behaviour; however the baryonic component does not show the same level of self-similarity. This picture is confirmed by X-ray observations, see for instance the deviation of the $L - T$ relation in clusters, which is steeper than the theoretical value predicted by the previous scenario. These deviations from self-similarity have been interpreted as the effects of non-gravitational heating due to radiative cooling as well as the energy injection from supernovae, AGN, star formation or galactic winds (see, e.g., Tozzi & Norman 2001; Bialek et al. 2001; Borgani et al. 2002; Babul et al. 2002; Borgani et al. 2004; Brighenti & Mathews 2006) which make the gas less centrally concentrated and with a shallower profile in the external regions with respect the DM component. Consequently, the comparison of the self-similar scaling relations to observations allows us to evaluate the importance of the effects of the non-gravitational processes on the ICM physics.

For Y and y_Ω we have the following dependences on the cosmology:

$$E_z \Delta_z^{1/2} Y \propto \left(E_z^{-1} \Delta_z^{-1/2} y_0 \right) \left(E_z \Delta_z^{1/2} R_{\Delta_z} \right)^2, \quad (16)$$

and

$$E_z^{-1} \Delta_z^{-1/2} y_\Omega \propto E_z^{-1} \Delta_z^{-1/2} y_0, \quad (17)$$

respectively, where the factor $\Delta_z = 200 \times [1 + 82(\Omega_z - 1)/(18\pi^2) - 39(\Omega_z - 1)^2/(18\pi^2)]$, with $\Omega_z = \Omega_{0m}(1+z)^3/E_z^2$, accounts for evolution of clusters in an adiabatic scenario (Bryan & Norman 1998).

Assuming the spherical collapse model for the DM halo and the equation of hydrostatic equilibrium to describe the distribution of baryons into the DM potential well, in the self-similar model the cluster mass and temperature are related by:

$$E_z \Delta_z^{1/2} M_{\text{tot}} \propto T^{3/2}; \quad (18)$$

so we have $R_{\Delta_z} \propto (M/(\rho_{c,z} \Delta_z))^{1/3} \propto T^{1/2} E_z^{-1} \Delta_z^{-1/2}$. By setting $f_z \equiv E_z(\Delta_z/\Delta)^{1/2}$, from the previous equations we can easily obtain the following relations (see, e.g., Markevitch 1998; Allen & Fabian 1998; Ettori et al. 2004b; Arnaud et al. 2005; Diaferio et al. 2005; Vikhlinin et al. 2005; Kotov & Vikhlinin 2005):

$$f_z(Y) \propto (f_z^{-1} y_0)^{5/3}, \quad (19)$$

$$y_\Omega \propto y_0, \quad (20)$$

$$f_z^{-1} y_0 \propto T^{3/2}, \quad (21)$$

$$f_z^{-1} y_0 \propto f_z M_{\text{tot}}, \quad (22)$$

$$f_z^{-1} y_0 \propto (f_z^{-1} L)^{3/4}, \quad (23)$$

$$f_z Y \propto T^{5/2}, \quad (24)$$

$$f_z Y \propto (f_z M_{\text{tot}})^{5/3}, \quad (25)$$

$$f_z Y \propto (f_z^{-1} L)^{5/4}. \quad (26)$$

We also remember here that for galaxy clusters similar scaling laws exist also in the X-ray band (see, e.g., Ettori et al. 2004a; Arnaud et al. 2005; Kotov & Vikhlinin 2005; Vikhlinin et al. 2006):

$$f_z^{-1} L \propto T_{\text{gas}}^2, \quad (27)$$

$$f_z M_{\text{tot}} \propto T_{\text{gas}}^{3/2}, \quad (28)$$

$$f_z^{-1} L \propto (f_z M_{\text{tot}})^{4/3}, \quad (29)$$

$$f_z M_{\text{gas}} \propto T_{\text{gas}}^{3/2}, \quad (30)$$

$$f_z^{-1} L \propto (f_z M_{\text{gas}})^{4/3}. \quad (31)$$

In our work we have considered all the physical quantity at fixed overdensity ($\Delta_z = \Delta$), i.e. $f_z = E_z$ in the above equations.

3.2 Fitting the scaling relations

We describe here the method adopted to obtain the best-fitting parameters in the scaling relations. Since they are power-law relations, we carry out a log-log fit:

$$\log(Y) = \alpha + A \log(X), \quad (32)$$

where X and Y represent the independent and dependent variables, respectively (hereafter $Y|X$); α and A are the two free parameters to be estimated. However, in the considered scaling relations it is unclear which variable should be considered as (in)dependent. Moreover both X - and Y -data have errors due to measurement uncertainties, plus an intrinsic scatter. For these reasons, the ordinary least squares (OLS) minimization approach is not appropriate: in fact it does not take into account intrinsic scatter in the data, and it is biased when errors affect the independent variable. So we decided to use the BCES (Bivariate Correlated Errors and intrinsic Scatter) ($Y|X$) modification or the bisector modification BCES (Y, X) proposed by Akritas & Bershady (1996), for which the best-fit results correspond to the bisection of those obtained from minimizations in the vertical and horizontal directions. Both these methods are robust estimators that take into account both any intrinsic scatter and the presence of errors on both variables.

The results for the best-fit normalization α and slope A for the listed scaling relations are presented in Table 4, where we also report the values of the total scatter

$$S = \left[\sum_j (\log Y_j - \alpha - A \log X_j)^2 / \nu \right]^{1/2} \quad (33)$$

and of the intrinsic scatter \hat{S} calculated as:

$$\hat{S} = \left[\sum_j \left((\log Y_j - \alpha - A \log X_j)^2 - \epsilon_{\log Y_j}^2 \right) / \nu \right]^{1/2}, \quad (34)$$

where $\epsilon_{\log Y_j} = \epsilon_{Y_j} / (Y_j \ln 10)$, with ϵ_{Y_j} being the statistical error of the measurement Y_j , and ν is the number of degrees of freedom ($\nu = N - 2$, with N equal to total number of data).

Notice that in these fits the physical quantities (L , M_{tot} , M_{gas} , Y) refer to R_{2500} estimated through the mass estimates based on the RTM model.

3.3 On the evolution of the scaling relations

We can extend the previous analysis by investigating the redshift evolution of the scaling relations at $z > 0.1$. Note that only two objects are available at $z > 0.6$ and that all CC clusters are at redshift below 0.45. We parametrize the evolution using a $(1+z)^B$ dependence and put constraints on the value of B by considering a least-square minimization of the relation

$$\log(Y) = \alpha + A \log(X) + B \log(1+z). \quad (35)$$

This is obtained by defining a grid of values of B and looking for the minimum of a χ^2 -like function, defined as:

$$\chi^2 = \sum_j \frac{[\log Y_j - \alpha - A \log X_j - B \log(1+z_j)]^2}{\epsilon_{\log Y_j}^2 + \epsilon_{\alpha}^2 + A^2 \epsilon_{\log X_j}^2 + \epsilon_A^2 \log^2 X_j}; \quad (36)$$

the sum is over all data, and $\epsilon_{\log X} \equiv \epsilon_X / (X \ln 10)$ and $\epsilon_{\log Y} \equiv \epsilon_Y / (Y \ln 10)$ are related to the uncertainties on X and Y , respectively. The best-fit parameters values calculated by using this method are reported in Table 5. Again in these fits, which refer to same scaling relations presented in Table 4, the physical quantities (L , M_{tot} , M_{gas} , Y) refer to R_{2500} , and masses are computed by assuming the RTM model.

4 DISCUSSION OF THE RESULTS

We present here a general discussion of our results concerning the scaling relations. In particular we have chosen to consider both the whole sample (CC plus NCC objects) and the CC-only subsample: this is done to allow a more direct comparison of our results with most of the works present in the literature, which are based on CC-sources only. Moreover this allows also to obtain at the same time more general relations which can be useful for future much extended (X-ray and SZ) cluster surveys, in which the distinction between relaxed and unrelaxed systems will be not easy.

4.1 The X-ray-only scaling relations

In this section we consider the scaling relations involving quantities extracted from the X-ray data only. We start by examining the relation between M_{tot} and T , and finding in general a good agreement between our best-fitting slopes and the values expected in the self-similar model. Then we will consider the other X-ray relations, finding slopes which are steeper than expected from the self-similar model. In particular the $L - T$, $L - M_{\text{gas}}$ and $M_{\text{gas}} - T$ relations display deviations larger than 2σ , while for the $L - M_{\text{tot}}$ relation we found agreement between the observed slope and the expected one.

4.1.1 The $M_{\text{tot}} - T$ relation

Without any assumption for models on the gas density and (deprojected) temperature profile, we have supposed that the DM density profile is well described by an analytical model (RTM or NFW). Thanks to the results of numerical simulations, we know, indeed, sufficiently well the DM physics which is in fact very simple, only depending on the gravity, unlike the physics of the baryons, which is also affected by further sources of non-gravitational energy. Moreover we have removed the observational biases in the determination of the deprojected temperature (and consequently of the mass) by adopting the spectral-like temperature estimator (see Sect. 2.3). In this way we have a bias-free estimate of the deprojected temperature and, therefore, of the cluster mass. Below we focus our attention on T_{mw} , because it is directly related to the total energy of the particles and so comparable to the results of hydrodynamical simulations, unlike T_{ew} , which is affected by observational biases (see, e.g., Gardini et al. 2004; Mazzotta et al. 2004; Mathiesen & Evrard 2001).

First, we notice that the two different models for the DM profile give slightly different results. Nevertheless, at an overdensity of $\Delta = 2500$ the masses determined by using RTM are

Table 4. Best-fit parameters for the scaling relations computed by using the cluster quantities evaluated at R_{2500} ; masses are estimated using the RTM profile. For each relation we give the logarithmic slope A (compared to the theoretically expected value A^*), the normalization α , the intrinsic scatter \hat{S} and the logarithmic scatter of the data S . The results are given both for a subsample including the CC clusters (11 objects), and for the whole sample (24 objects). In the column “method”, symbols (1) and (2) indicate if the fit has been performed by adopting the BCES ($Y|X$) or BCES (Y, X) methods, respectively. With the notation $(y_{0,-4}, y_{\Omega}, Y_8), L_{44}, T_7, M_{14}$, we indicate the Compton parameter, the X-ray luminosity, the temperature and the mass, in units of (10^{-4} , mJy, 10^8 mJy Mpc 2), 10^{44} erg s $^{-1}$, 7 keV, $10^{14} M_{\odot}$, respectively.

relation ($Y - X$)	Cooling core clusters 11 objects				All clusters 24 objects				method
	A/A^*	α	\hat{S}	S	A/A^*	α	\hat{S}	S	
$f_z Y_8 - f_z^{-1} y_{0,-4}$	1.22(± 0.15)/1.67	-1.07(± 0.06)	0.090	0.113	1.19(± 0.20)/1.67	-0.91(± 0.06)	0.116	0.137	(1)
$y_{\Omega} - y_{0,-4}$	0.93(± 0.14)/1.00	0.61(± 0.04)	0.033	0.076	0.92(± 0.26)/1.00	0.66(± 0.08)	0.120	0.140	(1)
$f_z^{-1} y_{0,-4} - T_{\text{ew},7}$	2.21(± 0.32)/1.50	0.19(± 0.05)	0.138	0.154	2.06(± 0.23)/1.50	0.15(± 0.03)	0.123	0.141	(2)
$f_z^{-1} y_{0,-4} - f_z M_{\text{tot},14}$	1.25(± 0.30)/1.00	-0.50(± 0.22)	0.248	0.257	1.22(± 0.29)/1.00	-0.41(± 0.17)	0.211	0.222	(2)
$f_z^{-1} y_{0,-4} - f_z^{-1} L_{44}$	0.75(± 0.07)/0.75	-0.69(± 0.11)	0.156	0.170	0.61(± 0.05)/0.75	-0.48(± 0.07)	0.124	0.142	(2)
$f_z Y_8 - T_{\text{ew},7}$	2.74(± 0.23)/2.50	-0.83(± 0.03)	0.103	0.124	2.64(± 0.28)/2.50	-0.74(± 0.03)	0.139	0.157	(2)
$f_z Y_8 - f_z M_{\text{tot},14}$	1.56(± 0.29)/1.67	-1.70(± 0.21)	0.235	0.245	1.48(± 0.39)/1.67	-1.42(± 0.21)	0.288	0.297	(2)
$f_z Y_8 - f_z^{-1} L_{44}$	0.92(± 0.11)/1.25	-1.92(± 0.16)	0.183	0.196	0.81(± 0.07)/0.75	-1.58(± 0.10)	0.237	0.248	(2)
$f_z^{-1} y_{\Omega} - T_{\text{ew},7}$	1.98(± 0.46)/1.50	0.80(± 0.05)	0.143	0.158	2.15(± 0.45)/1.50	0.79(± 0.05)	0.167	0.182	(2)
$f_z^{-1} y_{\Omega} - f_z M_{\text{tot},14}$	1.12(± 0.31)/1.00	0.17(± 0.22)	0.239	0.249	1.07(± 0.17)/1.00	0.31(± 0.10)	0.278	0.288	(2)
$f_z^{-1} y_{\Omega} - f_z^{-1} L_{44}$	0.68(± 0.09)/0.75	-0.02(± 0.14)	0.160	0.174	0.74(± 0.10)/0.75	0.00(± 0.15)	0.233	0.244	(2)
$f_z^{-1} L_{44} - T_{\text{ew},7}$	2.98(± 0.53)/2.00	1.18(± 0.05)	0.182	0.183	3.37(± 0.39)/2.00	1.03(± 0.05)	0.220	0.221	(2)
$f_z^{-1} L_{44} - f_z M_{\text{tot},14}$	1.71(± 0.46)/1.33	0.24(± 0.32)	0.205	0.206	2.03(± 0.54)/1.33	0.08(± 0.32)	0.269	0.270	(2)
$f_z M_{\text{tot},14} - T_{\text{ew},7}$	1.74(± 0.25)/1.50	0.56(± 0.03)	0.000	0.098	1.69(± 0.40)/1.50	0.47(± 0.04)	0.044	0.142	(2)
$f_z M_{\text{tot},14} - T_{\text{mw},7}$	1.63(± 0.25)/1.50	0.54(± 0.04)	0.000	0.087	1.69(± 0.34)/1.50	0.45(± 0.03)	0.000	0.125	(2)
$f_z M_{\text{gas},13} - T_{\text{ew},7}$	1.94(± 0.21)/1.50	0.57(± 0.02)	0.083	0.086	2.09(± 0.23)/1.50	0.51(± 0.02)	0.107	0.110	(2)
$f_z^{-1} L_{44} - f_z M_{\text{gas},13}$	1.55(± 0.13)/1.33	0.30(± 0.09)	0.083	0.085	1.64(± 0.13)/1.33	0.19(± 0.09)	0.131	0.132	(2)

in perfect agreement with the ones determined by using NFW ($\alpha_{\text{RTM}}^{\text{CC}} = 0.540 \pm 0.037$ and $A_{\text{RTM}}^{\text{CC}} = 1.630 \pm 0.253$, $\alpha_{\text{NFW}}^{\text{CC}} = 0.546 \pm 0.035$ and $A_{\text{NFW}}^{\text{CC}} = 1.590 \pm 0.250$). At $\Delta = 500$ the situation becomes less clear, because for most of the clusters we needed to extrapolate from R_{spec} (corresponding to $\Delta \sim 1000$) up to $\Delta = 500$, being R_{spec} of order of $(1/3)$ – $(1/2)$ of the virial radius (roughly corresponding to $R_{2500} - R_{1000}$). Hereafter we consider only the RTM model, even if most of the results present in the literature are usually based on the NFW one.

Considering the whole sample, we find a normalization ($\alpha = 0.45 \pm 0.03$), which is ~ 10 (~ 5) per cent smaller than the value found by Allen et al. (2001) (Arnaud et al. (2005)), who only consider relaxed clusters. Our normalization ($\alpha = 0.54 \pm 0.04$) is instead ~ 10 (~ 15) per cent larger than the value of Allen et al. (Arnaud et al.) if we only consider the CC-only subsample. This suggests a different behaviour depending on the presence or not of a cooling core (see also the left panel Fig. 3): in fact we find that at $\Delta = 2500$ the normalization of the NCC subsample at $M_{2500} = 5 \times 10^{14} M_{\odot}$ (corresponding to our median value for the mass) is ≈ 10 per cent smaller than for the CC-only subsample; conversely at $\Delta = 500$ the two subsamples give consistent normalizations, but the robustness of this result is affected by the fact that in this case we have to extrapolate the mass profile out of the region covered by observational data.

Some other authors (e.g., Arnaud et al. 2005) prefer to mask out the central region (up to $0.1 \times R_{200}$) in the determination of the

mass profile. We have decided to check the effects of the inclusion of the cooling region in our analysis by comparing the values of the mass obtained by excluding or not the central 100 kpc in the determination of the best fit parameters of the RTM profile: we pointed out that accounting for the cooling region does not involve any systematic error on the determination of the mass, indeed we obtain more statistically robust results.

Consequently the disagreement between CC and NCC clusters is probably due to a different state of relaxation, namely that the former are more regular and with more uniform physical properties than the latter (De Grandi & Molendi 2002); this is true even if we have masked out the most evident substructures. Notice that the observed mismatch is only marginally statistically significant ($\sim 1 - 1.5\sigma$). For a couple of clusters, namely A520 and A2163, we find that the exclusion of the unrelaxed central regions avoids observational biases due to the presence of local substructures: in particular the mass of the first (second) object increases by a factor of ~ 2 (~ 1.5) when excluding the central 300 (360) kpc. For other clusters which are evidently unrelaxed, we did not find any convenient way to avoid possible biases: even after masking out the most visible substructures, the analysis of the density and de-projected temperature profiles still reveals the possible presence of local irregularities (a sort of local ‘jumps’ in the profiles), which are difficult to individuate in the brightness image.

At $\Delta = 2500$, the best fitting normalization obtained considering the whole sample is ~ 30 per cent below the

Table 5. Best-fit parameters for the redshift evolution of the scaling relations. Again, the quantities are evaluated at R_{2500} and masses are estimated by using the RTM profile. For each relation we list the redshift evolution parameter B , the logarithmic slope A (compared to the theoretically expected value A^*), the normalization α , the minimum value of the function χ^2 and the number of degrees of freedom (d.o.f.). The results are given both for a subsample including the CC-only clusters (11 objects), and for the whole sample (24 objects). With the notation $(y_{0,-4}, y_{\Omega}, Y_8), L_{44}, T_7, M_{14}$, we indicate the Compton parameter, the X-ray luminosity, the temperature and the mass, in units of $(10^{-4}, \text{mJy}, 10^8 \text{ mJy Mpc}^2), 10^{44} \text{ erg s}^{-1}, 7 \text{ keV}, 10^{14} M_{\odot}$, respectively.

relation ($Y - X$)	Cooling core clusters 11 objects				All clusters 24 objects			
	B	A/A^*	α	χ^2_{\min} (d.o.f.)	B	A/A^*	α	χ^2_{\min} (d.o.f.)
$f_z Y_8 - f_z^{-1} y_{0,-4}$	$2.36^{+0.64}_{-0.68}$	$1.02(\pm 0.09)/1.67$	$-1.24(\pm 0.04)$	15.9(8)	$0.76^{+0.28}_{-0.28}$	$1.15(\pm 0.08)/1.67$	$-1.00(\pm 0.03)$	87.8(21)
$y_{\Omega} - y_{0,-4}$	$-1.56^{+0.56}_{-0.60}$	$0.85(\pm 0.08)/1.00$	$0.80(\pm 0.04)$	5.1(8)	$-1.24^{+0.24}_{-0.24}$	$0.82(\pm 0.07)/1.00$	$0.83(\pm 0.03)$	88.6(21)
$f_z^{-1} y_{0,-4} - T_{\text{ew},7}$	$-2.12^{+0.96}_{-0.96}$	$2.41(\pm 0.25)/1.50$	$0.40(\pm 0.03)$	23.4(8)	$0.08^{+0.36}_{-0.32}$	$2.08(\pm 0.17)/1.50$	$0.12(\pm 0.02)$	82.4(21)
$f_z^{-1} y_{0,-4} - f_z M_{\text{tot},14}$	$-2.44^{+1.68}_{-2.52}$	$1.35(\pm 0.23)/1.00$	$-0.33(\pm 0.19)$	29.6(8)	$0.08^{+0.48}_{-0.48}$	$0.98(\pm 0.10)/1.00$	$-0.27(\pm 0.07)$	55.6(21)
$f_z^{-1} y_{0,-4} - f_z^{-1} L_{44}$	$0.04^{+0.48}_{-1.16}$	$0.69(\pm 0.05)/0.75$	$-0.57(\pm 0.07)$	48.0(8)	$-0.32^{+0.16}_{-0.16}$	$0.62(\pm 0.03)/0.75$	$-0.44(\pm 0.05)$	99.7(21)
$f_z Y_8 - T_{\text{ew},7}$	$-1.08^{+1.12}_{-1.96}$	$2.98(\pm 0.31)/2.50$	$-0.71(\pm 0.04)$	10.6(8)	$0.28^{+0.40}_{-0.40}$	$2.66(\pm 0.20)/2.50$	$-0.78(\pm 0.03)$	37.9(21)
$f_z Y_8 - f_z M_{\text{tot},14}$	$-2.32^{+1.96}_{-2.60}$	$1.68(\pm 0.25)/1.67$	$-1.55(\pm 0.20)$	20.5(8)	$0.28^{+0.52}_{-0.52}$	$1.14(\pm 0.13)/1.67$	$-1.26(\pm 0.08)$	78.9(21)
$f_z Y_8 - f_z^{-1} L_{44}$	$2.40^{+0.44}_{-0.48}$	$0.70(\pm 0.05)/1.25$	$-1.81(\pm 0.07)$	58.9(8)	$0.12^{+0.20}_{-0.16}$	$0.62(\pm 0.04)/0.75$	$-1.35(\pm 0.05)$	206.0(21)
$f_z^{-1} y_{\Omega} - T_{\text{ew},7}$	$-4.00^{+0.96}_{-0.96}$	$2.31(\pm 0.26)/1.50$	$1.20(\pm 0.03)$	16.6(8)	$-1.44^{+0.36}_{-0.32}$	$1.95(\pm 0.18)/1.50$	$0.97(\pm 0.02)$	71.2(21)
$f_z^{-1} y_{\Omega} - f_z M_{\text{tot},14}$	$-4.88^{+1.68}_{-2.44}$	$1.33(\pm 0.22)/1.00$	$0.52(\pm 0.18)$	26.9(8)	$-1.52^{+0.44}_{-0.40}$	$0.82(\pm 0.12)/1.00$	$0.64(\pm 0.08)$	120.0(21)
$f_z^{-1} y_{\Omega} - f_z^{-1} L_{44}$	$-1.52^{+0.48}_{-0.44}$	$0.58(\pm 0.05)/0.75$	$0.34(\pm 0.07)$	47.5(8)	$-1.72^{+0.16}_{-0.16}$	$0.40(\pm 0.03)/0.75$	$0.65(\pm 0.05)$	178.0(21)
$f_z^{-1} L_{44} - T_{\text{ew},7}$	$-0.72^{+0.96}_{-1.00}$	$3.27(\pm 0.29)/2.00$	$1.25(\pm 0.03)$	69.40(8)	$0.92^{+0.52}_{-0.52}$	$4.05(\pm 0.24)/2.00$	$0.85(\pm 0.03)$	190.0(21)
$f_z^{-1} L_{44} - f_z M_{\text{tot},14}$	$-1.32^{+1.24}_{-1.56}$	$1.29(\pm 0.16)/1.33$	$0.66(\pm 0.13)$	5.4(8)	$-0.24^{+0.56}_{-0.56}$	$1.36(\pm 0.11)/1.33$	$0.53(\pm 0.07)$	40.5(21)
$f_z M_{\text{tot},14} - T_{\text{ew},7}$	$0.56^{+1.12}_{-1.20}$	$1.79(\pm 0.30)/1.50$	$-1.00(\pm 0.28)$	11.1(8)	$-0.08^{+0.52}_{-0.52}$	$2.30(\pm 0.24)/1.50$	$-1.51(\pm 0.22)$	48.4(21)
$f_z M_{\text{tot},14} - T_{\text{inw},7}$	$-0.88^{+1.24}_{-1.32}$	$2.00(\pm 0.28)/1.50$	$-1.09(\pm 0.27)$	7.1(8)	$-0.32^{+0.48}_{-0.48}$	$2.32(\pm 0.22)/1.50$	$-1.54(\pm 0.21)$	33.0(21)
$f_z M_{\text{gas},13} - T_{\text{ew},7}$	$0.16^{+0.56}_{-0.60}$	$2.00(\pm 0.16)/1.50$	$0.57(\pm 0.02)$	39.2(8)	$0.84^{+0.28}_{-0.28}$	$2.17(\pm 0.12)/1.50$	$0.41(\pm 0.02)$	127.0(21)
$f_z^{-1} L_{44} - f_z M_{\text{gas},13}$	$-0.92^{+0.24}_{-0.24}$	$1.43(\pm 0.03)/1.33$	$0.45(\pm 0.03)$	73.7(8)	$-0.60^{+0.12}_{-0.12}$	$1.63(\pm 0.02)/1.33$	$0.26(\pm 0.02)$	358.0(21)

value found in the non-radiative hydrodynamic simulations by Mathiesen & Evrard (2001)¹; for the CC-only subsample, the normalization is ~ 20 per cent below the theoretical value. The discrepancy is slightly reduced ($\sim 15 - 20$ per cent) with respect to the adiabatic hydrodynamic simulations by Evrard et al. (1996).

The picture emerging from numerical simulations with a more sophisticated ICM modeling is different. The simulation by Borgani et al. (2004), which includes radiative processes, supernova feedback, galactic winds and star formation, suggests a normalization which is in rough agreement with our whole sample, and 15 per cent lower with respect to the CC-only subsample. Notice, however, that the re-analysis of the same simulation data made by Rasia et al. (2005), who adopted a different definition of temperature, the spectroscopic-like one (which is not consistent with our definition of mass-weighted temperature; see above for a more detailed discussion), gives a higher ($\sim 40 - 50$ per cent) normalization.

Finally we notice that the slope of the $M - T$ relation is, indeed, in agreement with the theoretical expectations ($A^* = 1.5$).

Considering the results at an overdensity of 500, we found a good agreement (at 1σ level) between observed and theoretical slopes.

Our analysis suggests no evolution ($B^{\text{CC}} = -0.88^{+1.24}_{-1.32}$,

$B^{\text{all}} = -0.32 \pm 0.48$), in agreement with the literature (see, e.g., Finoguenov et al. 2001; Ettori et al. 2004b; Allen et al. 2001).

We compare also our intrinsic scatter, which is consistent with zero, with the one estimated by Rasia et al. (2005): they find a scatter of $\approx 30(16)$ per cent by considering the emission-weighted (spectroscopic-like) temperature. We reach similar conclusions comparing our intrinsic scatter with the value retrieved by Motl et al. (2005).

4.1.2 The $L - T$ relation

We find (see the upper-right panel of Fig. 3) a marginal agreement of our results on the slope of this relation ($A^{\text{all}} = 3.37 \pm 0.39$), with those obtained by Ettori et al. (2002), who found $A = 2.64 \pm 0.64$ at $\Delta = 2500$: however, their sample contains colder objects, for which a flatter relation would be expected. Our results also agree with the analysis made by Markevitch (1998): $A = 2.64 \pm 0.27$. Notice that his cluster sample is not directly comparable with ours, since it covers different ranges in redshift and temperature.

We compare our results about the scatter ($\hat{S} = 0.220$ and $S = 0.221$) with those obtained by Markevitch (1998), who found a smaller value: $S = 0.103$ (see, however, the previous comments on the different characteristics of the two samples).

Moreover, we find (at $\sim 1\sigma$) a positive (negative) redshift evolution for all clusters (CC-only subsample), i.e. we notice a mildly different behaviour on the evolution CC and NCC clusters.

¹ We have rescaled their results from $\Delta = 500$ to $\Delta = 2500$.

For comparison Ettori et al. (2002) found $B = -1.04 \pm 0.32$ for their sample of clusters at higher redshift.

Regarding the normalization we observe a slightly different behaviour when the CC-only subsample and whole sample are considered: $\alpha^{\text{CC}} = 1.18 \pm 0.05$ and $\alpha^{\text{all}} = 1.03 \pm 0.05$, respectively. We notice that the luminosity of the CC clusters is systematically larger than that of the NCC clusters, even if we have corrected it for the cooling flow (see Sect. 2.4), as already observed by Fabian (1994). On the contrary numerical simulations predict that the removal of the gas from the X-ray emitting phase reduces the luminosity (Muanwong et al. 2002). This confirms that cooling (Bryan 2000; Voit & Bryan 2001) is not effective in removing baryons from the X-ray phase, because of the presence of an extra-source of feedback or pre-heating (Balogh et al. 1999; Cavaliere et al. 1998; Tozzi & Norman 2001; Babul et al. 2002), which maintains the ICM at warm temperature (Borgani et al. 2002). Alternatively, the more evident negative evolution of the CC clusters compared to the NCC ones (especially in the y_Ω -X-ray(SZ) relations) could indicate different states of relaxation, being the former more regular, relaxed and virialized than the latter (De Grandi & Molendi 2002).

4.1.3 Other X-ray scaling relations

Here we discuss our results for the relations not shown in the figures. For the $M_{\text{gas}} - T$ relation we find a $\sim 1\sigma$ discrepancy between the slope of this relation in the CC-only subsample ($A^{\text{CC}} = 1.94 \pm 0.21$ and $A^{\text{all}} = 2.09 \pm 0.23$) and the theoretical expectation for the self-similar model ($A = 1.5$). Nevertheless, our estimate is consistent with the results already present in the literature. By applying a β -model to recover the gas mass, Vikhlinin et al. (1998) measured $A = 1.71 \pm 0.23$ at the baryon overdensity 1000 (approximately corresponding to the virial DM overdensity). Our slope is also in good agreement with the value ($A = 1.98 \pm 0.18$) found by Mohr et al. (1999), always by applying the β -model. We have also a marginal agreement (at 1σ level) with the value found by Ettori et al. (2004b) ($A = 2.37 \pm 0.24$), who make use of the β -model and apply the correction for E_z . Finally Ettori et al. (2002), combining a spectral analysis and the application of a β -model to the brightness distribution and without correcting for E_z , found $A = 1.91 \pm 0.29$ for $\Delta = 2500$ and $A = 1.74 \pm 0.22$ at $\Delta = 500$. The results of this last paper also suggest a low intrinsic scatter, in good agreement with our analysis ($\hat{S} = 0.079$). We point out here that we find some differences between CC and NCC clusters at $\Delta = 2500$, because of the contribution of the cooling core region ($\lesssim 100$ kpc); at $\Delta = 500$ this effect becomes negligible because the behaviour of the gas mass is dominated by the contribution from the external regions ($M_{\text{gas}} \propto r$). Finally no significant evolution is observed ($B = 0.16^{+0.56}_{-0.60}$) for the CC clusters; when we consider the whole sample, we notice a more significant positive evolution ($B = 0.84 \pm 0.28$).

Regarding the $L - M_{\text{tot}}$ the best-fit slope for the CC-only subsample ($A^{\text{CC}} = 1.71 \pm 0.46$) is in good agreement with the results obtained by Reiprich & Böhringer (2002) ($A = 1.80 \pm 0.08$), Ettori et al. (2002) ($A = 1.84 \pm 0.23$) and Ettori et al. (2004b) ($A = 1.88 \pm 0.42$). The observed scatter we measure ($S^{\text{CC}} = 0.206$, $S^{\text{all}} = 0.270$) is slightly smaller than in previous analysis by Reiprich & Böhringer (2002) ($S = 0.32$), and in agreement with Ettori et al. (2002) ($S = 0.26$). This seems to suggest that the methods we applied to correct the observed luminosity (see Sect. 2.4) and to determine the total mass are quite robust.

Hints of negative evolution are observed ($B^{\text{CC}} = -1.32^{+1.24}_{-1.56}$, $B^{\text{all}} = -0.24 \pm 0.56$).

For the $L - M_{\text{gas}}$ law we measure a slope which is discrepant with respect to the theoretical value expected in the self-similar model. This relation, together with the one between $M_{\text{gas}} - T$ and $M_{\text{tot}} - T$, has the lowest intrinsic scatter between the X-ray only scaling laws. Moreover we have a significant evidence of a negative redshift evolution.

4.2 The scaling relations involving the SZ effect

In this section, we discuss first the $Y - y_0$ and $y_\Omega - y_0$ relations, which are linking the SZ properties only (see Fig. 4), and then the relations between SZ and X-ray quantities (see Fig. 5). The importance of these relations relies on the possibility of providing new insights into the general physical properties of the ICM, in a way complementary to the X-ray view. In particular, the different dependence on the gas density and temperature of the SZ flux ($\sim n_e T$) with respect to the X-ray brightness ($\sim n_e^2 T^{1/2}$) can allow to reduce some of the biases present in the X-ray analysis. The presence of substructures and inhomogeneities in the ICM can indeed strongly affect some of the X-ray determined physical parameters, like temperature and luminosity. An independent approach through the SZ analysis of some physical quantities can shed more light on the limits of validity of the ICM self-similar scenario.

4.2.1 The $Y - y_0$, $y_\Omega - y_0$ relations

For both relations, we find slopes which are smaller than the expected ones. The discrepancy we measure is larger than the one found by McCarthy et al. (2003b). This is likely due to the fact that the self-similar model predicts a pressure profile which is steeper than the observed one: including extra-gravitational energy draws a picture in which the gas density (and consequently the pressure) has a profile shallower than the DM density. This is also confirmed by the observation that there are differences between CC (which are obviously more subject to non-gravitational processes) and NCC clusters, having the former a slightly ($\sim 1\sigma$) smaller integrated Compton parameter. We point out that the dispersion in these relations is very high, probably because of the systematics on the reconstruction of the integrated Compton parameter (see Sect. 2.5).

We measure a strong negative evolution in the $y_\Omega - y_0$ relation. As pointed out by McCarthy et al. (2003b), this different behaviour of the $y_\Omega - y_0$ relation (more in general of the y_Ω -X-ray and y_Ω -SZ relations) concerning the evolution is likely due to the fact the SZ effect within a fixed angular size samples larger physical region at higher redshifts. This means that the effect of non-gravitational processes are relatively more pronounced if the SZ flux is measured within smaller physical radii, where the density of the ICM is higher: this is expected in a scenario of either preheating, where we can assign a fixed extra-energy per particle, or cooling, where the radiative cooling is more prominent in the denser central regions. This is also in agreement with the general picture emerging by studying entropy profiles (Ponman et al. 2003; Pratt et al. 2006; Voit & Ponman 2003; Tozzi & Norman 2001), which is affected just in the central regions by non-gravitational processes, while the self-similarity is roughly preserved in the halo outskirts, where the dynamics is still dominated by the gravity.

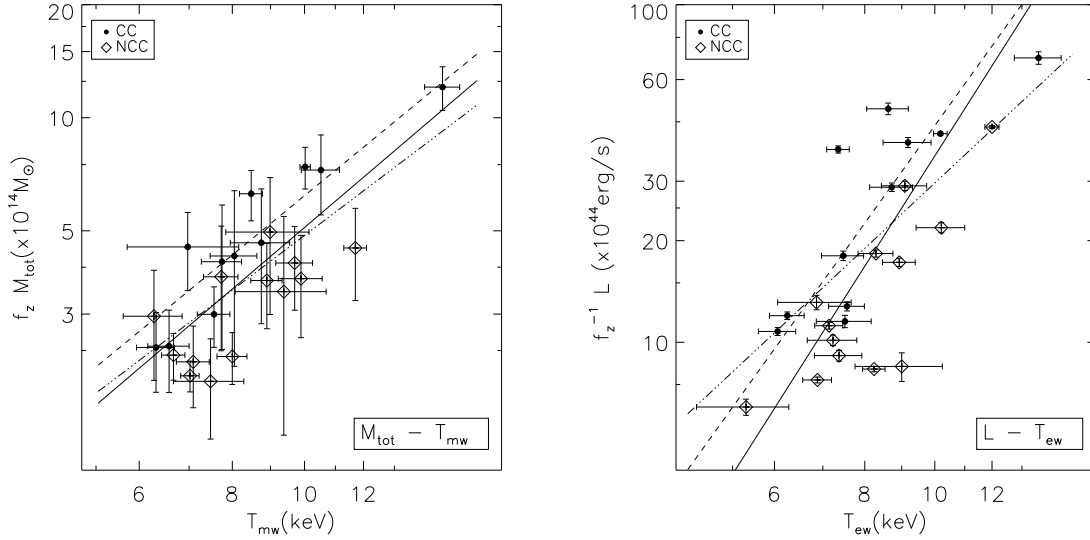


Figure 3. The relations between $M_{\text{tot}}-T_{\text{mw}}$ (left panel) and $L-T_{\text{ew}}$ (right panel). In each panel the filled circles represent cooling core (CC) sources, while the diamonds are the no-cooling core (NCC) ones. The solid line refers to the best-fit relation obtained when considering all clusters of our sample, the dashed one represents the best-fit when the CC sources only have been considered and the dot-dashed is the best-fit obtained by fixing the slope to the self-similar value.

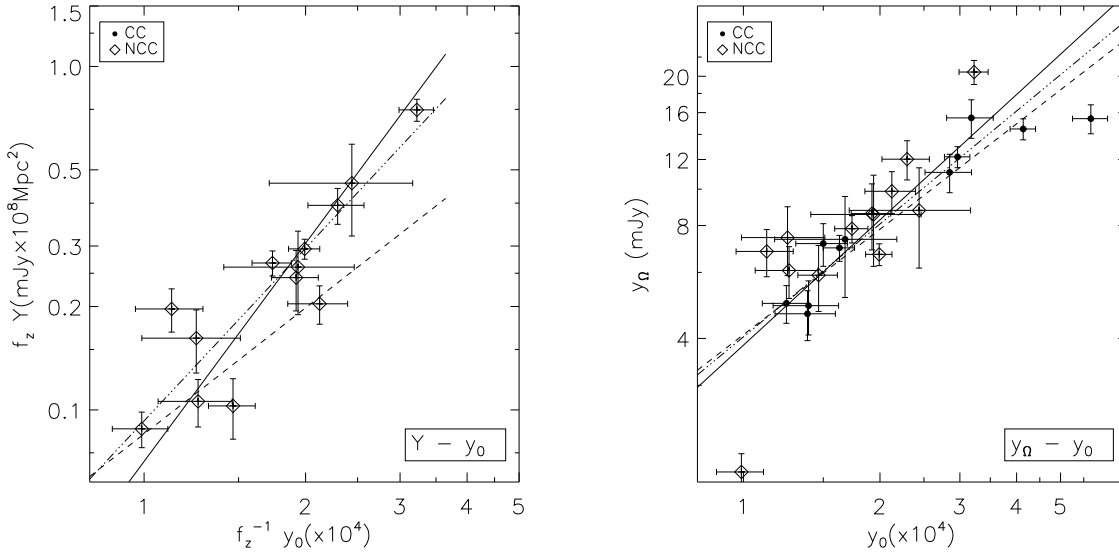


Figure 4. As in Fig. 3 but for the relations between $Y - y_0$ (left panel) and $y_{\Omega} - y_0$ (right panel).

4.2.2 The $y_0 - T$, $Y - T$, $y_{\Omega} - T$ relations

We note that $y_0 - T$ is the only scaling relation that deviates by $\gtrsim 3\sigma$ from the self-similar slope (see Table 4 and 5) both when only CC clusters and CC+NCC objects are considered. Moreover, we measure an higher normalization in the CC-only subsample, probably due to the inclusion of the cooling regions during the SZ data reduction and the subsequent fit in the visibility plane. These results, in good agreement with the ones presented in Benson et al. (2004), are consistently obtained with both a robust BCES fit and a χ^2 -minimization. By applying the former technique, this relation is also the one that shows the smaller scatter (both total and

intrinsic) around the best-fit. Furthermore, the χ^2 -approach indicates a significant negative evolution among the 11 CC clusters ($B^{\text{CC}} = -2.12^{+0.96}_{-0.96}$ at 2.5σ ; $\chi^2_{\text{min}} = 23.4$ with 8 d.o.f.) that disappears when the whole sample of 24 objects is considered. For the NCC sources we do observe hints of positive evolution ($B^{\text{NCC}} = 0.64^{+0.40}_{-0.40}$): this points to a different behaviour of the cool core and non-cool clusters in the central regions, and different state of relaxation of the gas as suggested by the comparison of the normalization of the fit ($\alpha^{\text{CC}} = 0.19 \pm 0.15$ and $\alpha^{\text{NCC}} = 0.14 \pm 0.35$).

The best-fitting relations for $Y - T$ show a value for the slope

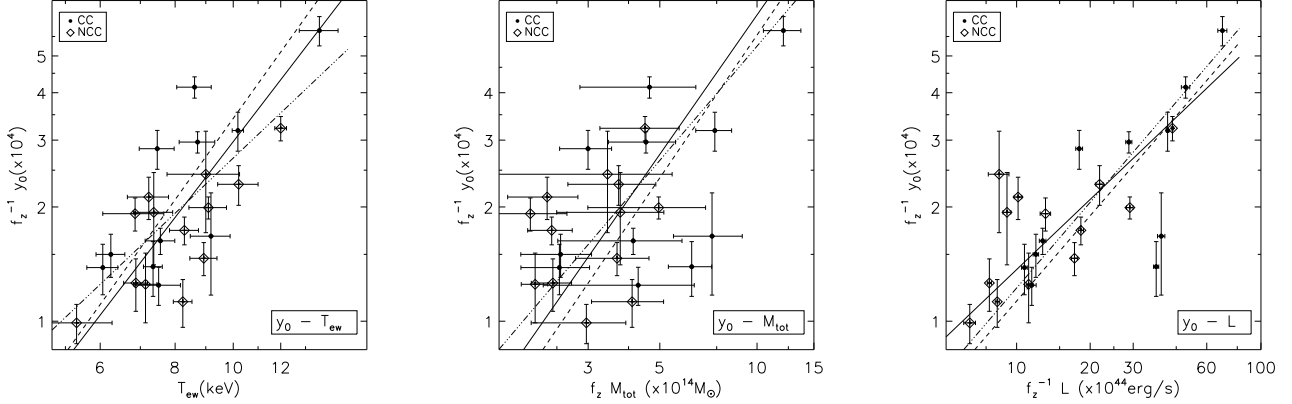


Figure 5. As in Fig. 3 but for the relations between $y_0 - T_{\text{ew}}$ (left panel), $y_0 - M_{\text{tot}}$ (central panel), $y_0 - L$ (right panel).

in agreement with the value predicted by the self-similar model either when we consider the CC-only clusters or the whole sample, unlike for the $y_0 - T$ relation: this is probably due to the sensitivity of y_0 to the cooling region. On the contrary for the $y_\Omega - T$ relation, when we consider the CC clusters, we observe a good agreement with the self-similar predictions ($A^{\text{CC}} = 1.98 \pm 0.46$ $A^* = 1.50$).

Our results confirms that the $Y - T$ relation exhibits a smaller scatter than the $y_0 - T$ one, as naively expected. Finally we find that the $y_\Omega - T$ relation has a larger scatter than the $Y - T$ one, in contrast with what obtained by McCarthy et al. (2003a). Moreover we notice in the CC-only subsample a mildly larger scatter compared to the whole cluster sample.

4.2.3 The $y_0 - M$, $Y - M$, $y_\Omega - M$ relations

These relations show a very good agreement between observed and self-similar slopes, with a scatter a factor of 2 larger than the correlation with T (see the previous subsection). We do not confirm the low scatter, $S \approx 10 - 15$ per cent, for the $Y - M$ relation suggested from the numerical simulations by Nagai (2006) and Motl et al. (2005): this indicate possible bias in the determination of Y . But it is possible that the present simulations are not completely adequate to reproduce the observed quantities, being the ICM modeling in hydrodynamical codes quite complex.

The normalization of the $Y - M_{\text{tot}}$ relation has been investigated in dedicated hydrodynamical simulations to discriminate between different ICM physics. For example, Nagai (2006) uses non-radiative (NR) and with gas cooling and star formation (CSF) simulated clusters to find a normalization that varies by about 70 per cent: for a typical cluster with $M_{2500} = 5 \times 10^{14} M_\odot$, $Y^{\text{NR}} = (1.32^{+0.10}_{-0.09}) \times 10^{-4}$ and $Y^{\text{CSF}} = (9.01^{+0.78}_{-0.59}) \times 10^{-5}$ at $z = 0^2$. At the same mass and overdensity, and fixing the slope to the self-similar model, our observed normalization is: $Y^{\text{CC}} = (5.32 \pm 1.06) \times 10^{-5}$ and $Y^{\text{all}} = (8.06 \pm 1.35) \times 10^{-5}$ for CC-only and all clusters, respectively. At $\Delta = 200$, the observed normalizations are $Y^{\text{CC}} = (1.30 \pm 0.74) \times 10^{-5}$ and $Y^{\text{all}} = (1.22 \pm 0.53) \times 10^{-5}$, systematically lower than the results in Nagai (2006) ($Y^{\text{NR}} = 5.13^{+0.57}_{-0.52} \times 10^{-5}$ and $Y^{\text{CSF}} = 3.95^{+0.37}_{-0.34} \times 10^{-5}$) and more in agreement with the results by da Silva et al. (2004),

that measure $Y^{\text{NR}} = 1.85 \times 10^{-5}$, $Y^{\text{cool}} = 1.73 \times 10^{-5}$ and $Y^{\text{pre-heat}} = 2.50 \times 10^{-6}$ for non-radiative, cooling (cool) and pre-heating (pre-heat) simulations, respectively.

We obtain, therefore, that our CC clusters, for which we obtain the most robust estimates of the total mass at the overdensity of 2500 (see Subsect. 4.1.1), well reproduce the distribution measured in the $Y - M_{\text{tot}}$ plane of the objects simulated including extra physical processes. Similar conclusions can be drawn for $Y - T_{\text{mw}}$ and $Y - L$ relations.

Finally, we find a negative evolution for the relations under examinations at $\gtrsim 1\sigma$ confidence level for the CC-only clusters (see Table 5). The slopes of the correlations tend, however, to deviate from the self-similar predictions more significantly than the measurements obtained with the robust fitting technique. If we fix the slope to the self-similar value A^* in these relations between SZ and X-ray quantities, we still obtain a negative evolution at $\approx 1 - 2\sigma$ confidence level. We note here that Nagai (2006), on the contrary, does not find any hint of evolution in the $Y - M$ relation.

4.2.4 The $y_0 - L$, $Y - L$, $y_\Omega - L$ relations

In general we find a good agreement between the best-fitted slope and the self-similar prediction. Compared to other scaling relations, in these cases the intrinsic scatter is very small (~ 0.15 for the $y_0 - L$ relation estimated in the CC-only subsample). We do not observe significant differences between CC and NCC clusters, being the estimates of luminosity corrected for the cooling core.

Regarding the evolution, we find suggestions (at 3σ level) for a negative evolution in the $y_\Omega - L$ relation ($B^{\text{CC}} = -1.52^{+0.48}_{-0.44}$). We observe instead positive evolution in the $Y - L$ relation, $B^{\text{CC}} = 2.40^{+0.44}_{-0.48}$, but negative evolution when we consider the NCC clusters ($B^{\text{NCC}} = -0.80^{+0.24}_{-0.20}$).

5 CONCLUSIONS

We have presented an analysis of X-ray and SZ scaling relations of a sample of 24 galaxy clusters in the redshift range 0.14-0.82, selected by having their SZ measurements available in literature. We have analyzed the Chandra exposures for these X-ray luminous objects. We have reconstructed their gas density, temperature and pressure profiles in a robust way. Then, we have investigated the

² Here we are following his definition of Y , corresponding to $I_0 = 1$ in eq.(11), and we adopt his cosmological parameters.

scaling relations holding between X-ray and SZ quantities. By assuming an adiabatic self-similar model, we have corrected the observed quantities by the factor $f_z \equiv E_z$, neglecting the factor Δ_z , checking that the final results do not change significantly in this way: so we can compare our results with the work in the literature. We have estimated the values of normalization, slope, observed and intrinsic scatters, and evolution to quantify the amplitude of the effects of the non-gravitational processes in the ICM physics. In this sense, the combined study of the SZ and X-ray scaling relations and their evolution in redshift is a powerful tool to investigate the thermodynamical history in galaxy clusters. Indeed, the departures from the self-similar predictions observed in some of the scaling laws studied in our work confirm that the simple adiabatic scenario is not wholly adequate to describe the physics of the X-ray luminous clusters, because it does not account for a further non-gravitational energy besides the potential one. We remind that our results are, by construction, more robust at R_{2500} , where no extrapolation is required and the determinations of the mass (at least for CC clusters) and the reconstruction of the integrated Compton parameter are reliable. These results can be here summarized as follows.

- We observe a good agreement of the normalization of the $M_{\text{tot}} - T$ relation between our results and the ones obtained in hydrodynamical numerical simulations. The other X-ray scaling relations involving a direct propagation of the absolute value of the measured gas density show a steeper slope than expected from self-similar predictions. Departures larger than 2σ are observed in the $L - T$ ($A^{\text{all}} = 3.37 \pm 0.39$ vs. $A^* = 2$), $L - M_{\text{gas}}$ ($A^{\text{all}} = 1.64 \pm 0.13$ vs. $A^* = 1.33$) and $M_{\text{gas}} - T$ ($A^{\text{all}} = 2.09 \pm 0.23$ vs. $A^* = 1.5$) relations. These results are consistent with previous analysis on high- z X-ray luminous galaxy clusters (see, e.g., Ettori et al. 2002; Kotov & Vikhlinin 2005; Maughan et al. 2006).

- Correlations between the investigated SZ quantities and the gas temperature have the largest deviations from the slope predicted from the self-similar model and the lowest scatter among similar relations with different X-ray quantities. The measured scatter is comparable to what is observed in the relations between X-ray parameters. The $Y - T$ relation shows the lowest total and intrinsic scatter both when CC clusters only and the whole sample are considered.

- We observe a strong negative evolution in the $y_\Omega - \text{X-ray}$ and $y_\Omega - \text{SZ}$ relations. A plausible explanation is that the SZ effect within a fixed angular size samples larger physical region at higher redshifts. That means the effect of non-gravitational processes are relatively more pronounced within smaller physical radii.

- The observed normalization of the $Y - M_{\text{tot}}$ relation in cooling-core clusters at $\Delta = 2500$, that provide the most robust estimates of the total masses in our cluster sample, agrees well with the predicted value from numerical simulations (see, e.g., da Silva et al. 2004; Nagai 2006). In particular, we confirm the trend that lower normalization are expected when some feedback processes take place in the cluster cores: for a cluster with typical $M_{2500} \approx 5 \times 10^{14} M_\odot$, we measure $Y^{\text{CC}} = (5.32 \pm 1.06) \times 10^{-5}$ in the sample of CC objects where the cooling activity is expected to be very effective, and $Y^{\text{all}} = (8.06 \pm 1.35) \times 10^{-5}$ in the whole sample. However, we have to note that the normalization in hydrodynamical simulations is strictly related to the adopted recipes to describe physical processes, like gas cooling and star formation. These processes are also responsible for the production of the cold baryon fraction, the amount of which is still under debate when

compared to the observational constraints (see, e.g., Borgani et al. 2006).

- The SZ – X-ray relations are, in general, well described by a self-similar model parametrized through the dependence upon f_z , when a robust fitting technique, that considers both the intrinsic scatter and the errors on the two variables, is adopted. On the contrary, when an evolution in the form $(1 + z)^B$ is investigated by a χ^2 -minimization with error propagations on both X and Y variables, we measure a strong negative evolution at $\gtrsim 1\sigma$ level of confidence for all relations that involve SZ quantities (y_0, Y, y_Ω) and the X-ray measured gas temperature and total mass. The slopes of the correlation tend, however, to deviate from the self-similar predictions more significantly than the measurements obtained with the robust fitting technique. If we fix the slope to the self-similar value A^* in these relations between SZ and X-ray quantities, we obtain stronger hints of negative evolution for the $y_0 - M_{\text{tot}}$ relation ($B^{\text{CC}} = -0.88 \pm 0.94$) and for the $Y - M_{\text{tot}}$ relation ($B^{\text{CC}} = -2.30 \pm 1.13$).

Our results on the X-ray and SZ scaling relations show a tension between the quantities more related to the global energy of the system (e.g. gas temperature, gravitating mass) and the indicators of the ICM structure (e.g. gas density profile, central Compton parameter y_0). Indeed, by using a robust fitting technique, the most significant deviations from the values of the slope predicted from the self-similar model are measured in the $L - T$, $L - M_{\text{tot}}$, $M_{\text{gas}} - T$, $y_0 - T$ relations. When the slope is fixed to the self-similar value, these relations show consistently a negative evolution suggesting a scenario in which the ICM at higher redshift has lower both X-ray luminosity and pressure in the central regions than the self-similar expectations. These effects are more evident in relaxed CC clusters in the redshift range 0.14-0.45, where a more defined core is present and the assumed hypotheses on the state of the ICM are more reliable.

A likely explanation is that we need an increase in the central entropy to spread the distribution of the gas on larger scales: this could be achieved either by episodes of non-gravitational heating due to supernovae and AGN (see, e.g., Evrard & Henry 1991; Cavaliere et al. 1999; Tozzi & Norman 2001; Bialek et al. 2001; Brighenti & Mathews 2001; Babul et al. 2002; Borgani et al. 2002), or by selective removal of low-entropy gas through cooling (see, e.g., Pearce et al. 2001; Voit & Bryan 2001; Wu & Xue 2002), possibly regulated by some mechanism supplying energy feedback [e.g. the semi-analytical approach proposed by Voit et al. (2002) and the numerical simulations discussed by Muanwong et al. (2002); Tornatore et al. (2003); Kay et al. (2003)].

ACKNOWLEDGEMENTS

We thank the anonymous referee for a careful reading of the manuscripts and suggestions that have improved the presentation of our work. We thank Steven Myers for useful discussions on SZ data and NRAO for the kind hospitality. The visit at NRAO has been partially supported also by the ‘Marco Polo’ program of University of Bologna. We acknowledge the financial support from contract ASI-INAF I/023/05/0 and from the INFN PD51 grant.

REFERENCES

- Akritas M. G., Bershadsky M. A., 1996, *ApJ*, 470, 706
- Allen S. W., Fabian A. C., 1998, *MNRAS*, 297, L57

- Allen S. W., Schmidt R. W., Fabian A. C., 2001, *MNRAS*, 328, L37
- Anders E., Grevesse N., 1989, *GeCoA*, 53, 197
- Arnaud K. A., 1996, in Jacoby G. H., Barnes J., eds, *ASP Conf. Ser. 101: Astronomical Data Analysis Software and Systems V XSPEC: The First Ten Years*. pp 17–
- Arnaud M., Pointecouteau E., Pratt G. W., 2005, *A&A*, 441, 893
- Babul A., Balogh M. L., Lewis G. F., Poole G. B., 2002, *MNRAS*, 330, 329
- Balogh M. L., Babul A., Patton D. R., 1999, *MNRAS*, 307, 463
- Benson B. A., Church S. E., Ade P. A. R., Bock J. J., Ganga K. M., Henson C. N., Thompson K. L., 2004, *ApJ*, 617, 829
- Bialek J. J., Evrard A. E., Mohr J. J., 2001, *ApJ*, 555, 597
- Birkinshaw M., 1999, *Phys. Rep.*, 310, 97
- Bonamente M., Joy M. K., LaRoque S. J., Carlstrom J. E., Reese E. D., Dawson K. S., 2006, *ApJ*, 647, 25
- Borgani S., Dolag K., Murante G., Cheng L.-M., Springel V., Diaferio A., Moscardini L., Tormen G., Tornatore L., Tozzi P., 2006, *MNRAS*, 367, 1641
- Borgani S., Governato F., Wadsley J., Menci N., Tozzi P., Quinn T., Stadel J., Lake G., 2002, *MNRAS*, 336, 409
- Borgani S., Murante G., Springel V., Diaferio A., Dolag K., Moscardini L., Tormen G., Tornatore L., Tozzi P., 2004, *MNRAS*, 348, 1078
- Brighenti F., Mathews W. G., 2001, *ApJ*, 553, 103
- Brighenti F., Mathews W. G., 2006, *ApJ*, 643, 120
- Bryan G. L., 2000, *ApJ*, 544, L1
- Bryan G. L., Norman M. L., 1998, *ApJ*, 495, 80
- Carlstrom J. E., Holder G. P., Reese E. D., 2002, *ARA&A*, 40, 643
- Cavaliere A., Fusco-Femiano R., 1976, *A&A*, 49, 137
- Cavaliere A., Menci N., Tozzi P., 1998, *ApJ*, 501, 493
- Cavaliere A., Menci N., Tozzi P., 1999, *MNRAS*, 308, 599
- Cooray, A. R. 1999, *MNRAS*, 307, 841
- da Silva A. C., Kay S. T., Liddle A. R., Thomas P. A., 2004, *MNRAS*, 348, 1401
- De Grandi S., Molendi S., 2002, *ApJ*, 567, 163
- Diaferio A., Borgani S., Moscardini L., Murante G., Dolag K., Springel V., Tormen G., Tornatore L., Tozzi P., 2005, *MNRAS*, 356, 1477
- Dickey J. M., Lockman F. J., 1990, *ARA&A*, 28, 215
- Ettori S., De Grandi S., Molendi S., 2002, *A&A*, 391, 841
- Ettori S., Borgani S., Moscardini L., Murante G., Tozzi P., Diaferio A., Dolag K., Springel V., Tormen G., Tornatore L., 2004a, *MNRAS*, 354, 111
- Ettori S., Tozzi P., Borgani S., Rosati P., 2004b, *A&A*, 417, 13
- Evrard A. E., Henry J. P., 1991, *ApJ*, 383, 95
- Evrard A. E., Metzler C. A., Navarro J. F., 1996, *ApJ*, 469, 494
- Fabian A. C., 1994, *ARA&A*, 32, 277
- Finoguenov A., Reiprich T. H., Böhringer H., 2001, *A&A*, 368, 749
- Gardini A., Rasia E., Mazzotta P., Tormen G., De Grandi S., Moscardini L., 2004, *MNRAS*, 351, 505
- Itoh N., Kohyama Y., Nozawa S., 1998, *ApJ*, 502, 7
- Kaastra J. S., 1992, *An X-Ray Spectral Code for Optically Thin Plasmas* (Internal SRON-Leiden Report, updated version 2.0)
- Kaiser N., 1986, *MNRAS*, 222, 323
- Kay S. T., Thomas P. A., Theuns T., 2003, *MNRAS*, 343, 608
- Kotov O., Vikhlinin A., 2005, *ApJ*, 633, 781
- Kriss G. A., Cioffi D. F., Canizares C. R., 1983, *ApJ*, 272, 439
- LaRoque S. J., Bonamente M., Carlstrom J. E., Joy M. K., Nagai D., Reese E. D., Dawson K. S., 2006, *ApJ*, 652, 917
- Liedahl D. A., Osterheld A. L., Goldstein W. H., 1995, *ApJ*, 438, L115
- Markevitch M., 1998, *ApJ*, 504, 27
- Mathiesen B. F., Evrard A. E., 2001, *ApJ*, 546, 100
- Maughan B. J., Jones L. R., Ebeling H., Scharf C., 2006, *MNRAS*, 365, 509
- Mazzotta P., Rasia E., Moscardini L., Tormen G., 2004, *MNRAS*, 354, 10
- McCarthy I. G., Babul A., Holder G. P., Balogh M. L., 2003a, *ApJ*, 591, 515
- McCarthy I. G., Holder G. P., Babul A., Balogh M. L., 2003b, *ApJ*, 591, 526
- McLaughlin D. E., 1999, *AJ*, 117, 2398
- Mohr J. J., Mathiesen B., Evrard A. E., 1999, *ApJ*, 517, 627
- Motl P. M., Hallman E. J., Burns J. O., Norman M. L., 2005, *ApJ*, 623, L63
- Muanwong O., Thomas P. A., Kay S. T., Pearce F. R., 2002, *MNRAS*, 336, 527
- Nagai D., 2006, *ApJ*, 650, 538
- Navarro J. F., Frenk C. S., White S. D. M., 1997, *ApJ*, 490, 493
- Pearce F. R., Jenkins A., Frenk C. S., White S. D. M., Thomas P. A., Couchman H. M. P., Peacock J. A., Efstathiou G., 2001, *MNRAS*, 326, 649
- Ponman T. J., Cannon D. B., Navarro J. F., 1999, *Nat*, 397, 135
- Ponman T. J., Sanderson A. J. R., Finoguenov A., 2003, *MNRAS*, 343, 331
- Pratt G. W., Arnaud M., Pointecouteau E., 2006, *A&A*, 446, 429
- Press W. H., Teukolsky S. A., Vetterling W. T., Flannery B. P., 1992, *Numerical recipes in C. The art of scientific computing*. Cambridge: University Press, —c1992, 2nd ed.
- Rasia E., Mazzotta P., Borgani S., Moscardini L., Dolag K., Tormen G., Diaferio A., Murante G., 2005, *ApJ*, 618, L1
- Rasia E., Tormen G., Moscardini L., 2004, *MNRAS*, 351, 237
- Reiprich T. H., Böhringer H., 2002, *ApJ*, 567, 716
- Rephaeli Y., Sadeh S., Shimon M., 2005, in Melchiorri F., Rephaeli Y., eds, *Background Microwave Radiation and Intra-cluster Cosmology The Sunyaev-Zeldovich effect*. pp 57–
- Sunyaev R. A., Zeldovich Y. B., 1970, *Comments on Astrophysics and Space Physics*, 2, 66
- Tornatore L., Borgani S., Springel V., Matteucci F., Menci N., Murante G., 2003, *MNRAS*, 342, 1025
- Tozzi P., Norman C., 2001, *ApJ*, 546, 63
- Vikhlinin A., Kravtsov A., Forman W., Jones C., Markevitch M., Murray S. S., Van Speybroeck L., 2006, *ApJ*, 640, 691
- Vikhlinin A., Markevitch M., Murray S. S., Jones C., Forman W., Van Speybroeck L., 2005, *ApJ*, 628, 655
- Vikhlinin A., McNamara B. R., Forman W., Jones C., Quintana H., Hornstrup A., 1998, *ApJ*, 502, 558
- Voit G. M., Bryan G. L., 2001, *Nat*, 414, 425
- Voit G. M., Bryan G. L., Balogh M. L., Bower R. G., 2002, *ApJ*, 576, 601
- Voit G. M., Ponman T. J., 2003, *ApJ*, 594, L75
- White M., Hernquist L., Springel V., 2002, *ApJ*, 579, 16
- Wu X.-P., Xue Y.-J., 2002, *ApJ*, 572, L19

APPENDIX A: SPECTRAL DEPROJECTION TECHNIQUE

The deprojection technique decomposes the observed X-ray emission of the i -th annulus into the contributions from the volume fraction of the j -th spherical shells with $j \leq i$, by fixing the spectrum

normalization of the outermost shell to the corresponding observed values. We can construct an upper triangular matrix \mathcal{V}_i^j , where the column vectors $\mathcal{V}^1, \mathcal{V}^2, \dots, \mathcal{V}^n$ represent the “effective” volumes, i.e. the volume of the j -th shell contained inside the i -th annulus (with $j \geq i$) and corrected by the gradient of n_e^2 inside the j -th shell (see Appendix B for more detail), so as:

$$K_i \propto \int_{j \geq i} n_{e,j}^2 dV = \left(\mathcal{V} \# \vec{n}_e^2 \right)_i. \quad (\text{A1})$$

In the previous equation $\vec{n}_e \equiv (n_{e,1}, n_{e,2}, \dots, n_{e,n})$, being n the total number of annuli, having internal (external) radius $r_{\text{in},1}, r_{\text{in},2}, \dots, r_{\text{in},n}$ ($r_{\text{out},1}, r_{\text{out},2}, \dots, r_{\text{out},n}$), with $n \sim 15 - 40$; K_i is the MEKAL normalization of the spectrum in the i -th annulus; the operator $\#$ indicates the matrix product (rows by columns). Notice that the integral $\int_{j \geq i} n_{e,j}^2 dV$ is of the order of the emission measure inside the i -th ring.³ The inversion of this matrix allows us to determine $n_{e,i}$.

The values of K_i are obtained by rescaling by the observed number of counts in the i -th ring the faked *Chandra* spectrum with absorption, temperature and metallicity measured in that ring. The errors are computed by performing 100 Monte Carlo simulations of the observed counts. We pointed out that the uncertainties in the estimates of the projected temperature do not reflect into high systematic errors in the determination of K_i , because of the mild dependence on T of the cooling function $\Lambda(T)$ integrated in the considered band (0.5 – 5 keV): $\Lambda(T) \propto T^{-\alpha}$, with $0.1 \lesssim \alpha \lesssim 0.2$ for $T \sim 7 - 12$ keV.

This approach is very powerful, because does not require any “real” spectral analysis, which could suffer of the poorness of the statistics and would need at least ~ 2000 net counts per annulus: we can determine the projected density in annuli even with very small counts ($\sim 200 - 1000$). In other words we have an improvement (of about one order of magnitude) of the spatial resolution in the spectral analysis.

Concerning the temperature analysis, we have determined its value T_j in the j -th shell, by assuming analytic relations for the mass density profiles: $\rho = \rho(\mathbf{r}, \mathbf{q})$, where $\mathbf{q} = (q_1, q_2, \dots, q_h)$ are suitable parameters. As discussed in Section 2.4, we consider two functional forms, a NFW profile with $\mathbf{q} \equiv (c, r_s)$ and a RTM profile with $\mathbf{q} = (x_s^*, r_{\text{vir}})$.

We performed a spectral deprojection of the observed temperature T_{shell}^* in a set of n^* annuli with width much larger than the previous ones, with internal (external) radius $r_{\text{in},1}^*, r_{\text{in},2}^*, \dots, r_{\text{in},n^*}^*$ ($r_{\text{out},1}^*, r_{\text{out},2}^*, \dots, r_{\text{out},n^*}^*$) corresponding to the ones of the rings in which we have estimated the projected temperature (see Sect. 2.2), with $n^* \ll n$ ($n^* \sim 3 - 8$), so as to have at least 2000 counts per annulus. The deprojection method works in this way:

$$\vec{T}_{\text{ring},m} = \left(\mathcal{V}^* \# \left(\vec{T}_{\text{shell}}^* \cdot \vec{\epsilon}^* \right) \right)_{\text{m}} / L^*_{\text{ring},m}, \quad (\text{A2})$$

where the operator “ \cdot ” indicates the product: $\vec{T}_{\text{shell}}^* \cdot \vec{\epsilon}^* = (T_{\text{shell},1}^* \epsilon_1^*, T_{\text{shell},2}^* \epsilon_2^*, \dots, T_{\text{shell},n^*}^* \epsilon_{n^*}^*)$. In eq.(A2), $\epsilon^* = \mathcal{V}^{*-1} \# \vec{L}_{\text{ring}}$ is the emissivity, $\mathcal{V}^* = [\mathcal{V}^1, \mathcal{V}^2, \dots, \mathcal{V}^{n^*}]$, $L^*_{\text{ring},m}$ is the luminosity of the m -th ring,⁴ and the generic parameter \mathcal{P}^*

³ Hereafter we assume that the index j (i) indicates the shell (ring) of the source of radius ($r_{\text{in}}, r_{\text{out}}$).

⁴ Hereafter we assume that the index k (m) indicates the shell (ring) having radius ($r_{\text{in}}^*, r_{\text{out}}^*$).

has the same meaning as above, but it is evaluated in n^* annuli. The inversion of the matrix in eq.(A2) allows us to finally estimate the deprojected temperature T_k^* .

We computed the theoretical temperature T_j by numerically integrating the equation of the hydrostatic equilibrium (eq. 1), assuming spherical geometry ($\vec{r} \equiv r$). Then we constructed a grid of values for P_0 and for the parameters \mathbf{q} entering the DM density profiles, so as $T_j = T_j(\mathbf{q}, P_0)$. In particular for P_0 we have considered the range $\hat{P}_0 - 3\sigma_{P_0} \leq P_0 \leq \hat{P}_0 + 3\sigma_{P_0}$, where \hat{P}_0 is the expectation value of P_0 . So we can estimate the temperature $kT_j(\mathbf{q}, P_0) = P(r)/n_{\text{gas}}(r)$.

Since the temperature $T_j(\mathbf{q}, P_0)$ obtained in this way is given on a set of n annuli with spatial resolution much better than the deprojected temperature $T_{\text{shell},k}^*$ defined in the n^* annuli only, we perform a (gas mass-weighted) average to calculate the temperature $T_k^{\text{ave}}(\mathbf{q}, P_0)$ in the k -th shell:

$$T_k^{\text{ave}}(\mathbf{q}, P_0) = \frac{\sum_{r_k \leq r_j < r_{k+1}} w_j T_j(\mathbf{q}, P_0) dV_j}{\sum_{r_k \leq r_j < r_{k+1}} w_j dV_j}, \quad (\text{A3})$$

where $w_j = n_j$ and dV_j represents the volume of the j -th shell, so as to reproduce a mass-weighted temperature. A χ^2 -minimization between $T_k^{\text{ave}}(\mathbf{q}, P_0)$ and $T_{\text{shell},k}^*$ (with error $\sigma_{T_{\text{shell},k}^*}$),

$$\chi^2 = \sum_{k=1}^{n^*} (T_k^{\text{ave}}(\mathbf{q}, P_0) - T_{\text{shell},k}^*)^2 / \sigma_{T_{\text{shell},k}^*}^2 \quad (\text{A4})$$

provides us the best estimate of (\mathbf{q}, P_0) .

We also considered an alternative approach to determine (\mathbf{q}, P_0) . Following Mazzotta et al. (2004), we perform a weighted average of $T_k(\mathbf{q}, P_0)$ to compute a projected spectral-like temperature $T_{\text{proj},m}(\mathbf{q}, P_0)$ in the m -th ring to be compared with the observed temperature $T_{\text{proj},m}^*$ of the m -th ring:

$$T_{\text{proj},m}(\mathbf{q}, P_0) = \left(\tilde{\mathcal{V}}^* \# \left(\vec{T}^{\text{ave}}(\mathbf{q}, P_0) \cdot \vec{w}(\mathbf{q}, P_0) \right) \right)_{\text{m}} / \mathcal{L}_{\text{ring},m}, \quad (\text{A5})$$

where $w_j = n_j^2 T_j^{-\alpha}(\mathbf{q}, P_0)$, $\alpha = 3/4$, $\vec{\mathcal{L}}_{\text{ring}}(\mathbf{q}, P_0) = \tilde{\mathcal{V}}^* \# \vec{w}(\mathbf{q}, P_0)$; $\tilde{\mathcal{V}}^* = [\mathcal{V}^1, \mathcal{V}^2, \dots, \mathcal{V}^{n^*}, \mathcal{V}^{n^*+1}, \dots, \mathcal{V}^{n^*+h}]$ is an extension of the volume matrix \mathcal{V}^* which takes into account the contributions (up to a distance of 10 Mpc) coming from the h annuli external to R_{spat} . We have to use the following fitting function, which is a simplified of the functional form of Vikhlinin et al. (2005):

$$n_e(r) = \frac{n_0 (r/r_c)^{-\alpha} (1 + r^\gamma/r_s^\gamma)^{-\epsilon/\gamma}}{(1 + r^2/r_c^2)^{3/2} \beta^{-\alpha/2}} \quad (\text{A6})$$

with $\gamma = 3$, and (1) to extrapolate $n_e(R)$, the pressure and temperature in regions outside R_{spat} . Notice that the previous definition of temperature is a very powerful way to remove observational biases: in fact we are weighting different regions along the line of sight using different temperatures which are obtained by performing a spectral fit of a single-temperature model. With this approach we have a robust determination of the deprojected temperature profile. The best estimate of (\mathbf{q}, P_0) is obtained through a χ^2 -minimization between $T_{\text{proj},m}(\mathbf{q}, P_0)$ and $T_{\text{proj},m}^*$:

$$\chi^2 = \sum_{m=1}^{n^*} \frac{(T_{\text{proj},m}(\mathbf{q}, P_0) - T_{\text{proj},m}^*)^2}{\sigma_{T_{\text{proj},m}^*}^2 + \sigma_{T_{\text{proj},m}}^2}. \quad (\text{A7})$$

Here $\sigma_{T_{\text{proj},m}}^2$ accounts for the statistical errors in eq.(1) coming from the measured errors for $n_{\text{gas}}(r)$. The reduced χ^2 resulting

from this method is better than in previous case: this is likely due to the fact that the deprojected temperature T_{shell}^* strongly relies on assumptions, like spherical symmetry and uniform density profile, which are not completely satisfied in real clusters. Moreover the values of $T_{\text{shell},k}^*$ are not independent: in fact we relate the deconvolved temperature, gas density and spectra normalization of the outermost shell to its observed values and then we compute the physical parameters in the m -th annulus by opportunely accounting for the contributions of the k -th shell ($k \geq m$): this could propagate possible systematic errors from the external regions, where the determination of the physical properties cannot be so adequate because of the bad statistic. All the deprojected quantities presented in the present work refer to the second approach (T_{proj}) only.

APPENDIX B: DETERMINING THE EFFECTIVE VOLUME

Kriss et al. (1983) computed the geometrical volume of the j -th shell intercepted by the i -th annulus (with $j \geq i$) as:

$$V_i^j = 4\pi \int_{r_{\text{in}_i}}^{r_{\text{out}_i}} dr r \int_{(r_{\text{out}_j}^2 - r^2)^{1/2}}^{(r_{\text{in}_j}^2 - r^2)^{1/2}} dz. \quad (\text{B1})$$

Notice that when we use a geometrical volume to deproject the physical parameters (like the density as example) we are assuming that they are nearly constant in the shell. This introduces a systematic bias in the deprojected quantity, that tends to be increased when the gradient of the physical parameter is not negligible or when the rings are wide. McLaughlin (1999) partially corrected this bias by referring the density to an average radius, $r_{\text{ave}} \equiv ((r_{\text{out}}^{3/2} + r_{\text{in}}^{3/2})/2)^{2/3}$.

Here we introduce a new definition of the volume, the effective volume \mathcal{V} , which takes into account the real gradient of the physical parameters as a function of the radius. We assumed that we are weighting the unknown physical parameter \mathcal{P} in the j -th shell using a function $w(R)$, whose gradient is only due to the case of the squared density ($w(R) \propto n_e^2$).

We have modeled the density inside the j -th shell as a local power-law, $n(R) = n_{e,j} f(R)^{-\alpha}$, where $f(R) = (R/r_{\text{ref}_j})$, $r_{\text{ref}_j} \equiv (r_{\text{in}_j} + r_{\text{out}_j})/2$, $\alpha(R) = -\log(n^{j+1}/n^j)/\log(r_{\text{ref}_{j+1}}/r_{\text{ref}_j}) + \mathcal{O}(\alpha)$. We first calculated $\alpha(R)$ by relying on the initial density obtained from the geometric volume-deprojection on a radius r_{ref_j} : in this way the introduced errors on α are negligible ($\mathcal{O}(\alpha)$).

We define r as the projection of R on the sky plane, with $R^2 = r^2 + z^2$, being z the distance along the line of the sight. So, if $n(r_{\text{ref}_j})$ is the density in the j -th shell, the observed parameter \mathcal{P}^* is related to the theoretical one by:

$$\begin{aligned} \vec{P}^* &= \int dV \vec{P} w(R) = \int dV \vec{P} n_e^2(R) = \\ &= \left(\int dV f(R)^{-2\alpha} \right) \# \left(n_{e,j}^2 \vec{P} \right) = \mathcal{V} \# \left(n_{e,j}^2 \vec{P} \right). \end{aligned} \quad (\text{B2})$$

So we can re-write the effective volume \mathcal{V} as:

$$\mathcal{V}_i^j = \int_{j \geq i} dV f(R)^{-2\alpha} = 4\pi \int_{r_{\text{in}_i}}^{r_{\text{out}_i}} dr r \int_{(r_{\text{out}_j}^2 - r^2)^{1/2}}^{(r_{\text{in}_j}^2 - r^2)^{1/2}} dz f(R)^{-2\alpha}. \quad (\text{B3})$$

The effective volume \mathcal{V}_i^j is equal to the geometric one V_i^j if $\alpha = 0$, i.e. when we have negligible gradients of $n(R)^2$ in the j -th shell. This is approximately true only in the case in which we have

a good spatial resolution, for example when we consider n annuli ($n \sim 15 - 40$) in the brightness image (see Section 2.3). But this is false when we have n^* annuli, with $n^* \ll n$ ($n^* \sim 3 - 8$) in the spectral analysis, for which a larger statistics (at least ~ 2000 net counts per annulus) is required. In this last case, for example, it is possible to underestimate the true density in the external regions by 5 – 10 per cent by using the geometrical volume instead of the effective one: this corresponds to set \vec{P} equal to \mathcal{I} (being \mathcal{I} the identity matrix) in eq.(B2), and $\vec{P}^* \propto K$ (see eq. A1). The analysis we performed shows that the case in which adopting the effective volume is important is in eq.(A2): using an effective volume can avoid to introduce systematic errors in the determination of the cluster masses.